Uncertainty Reduction in Diffusion Magnetic Resonance Imaging Tractography

Kumulative Dissertation

zur Erlangung des Doktorgrades (Dr. rer. nat.)
der
Mathematisch-Naturwissenschaftlichen Fakultät
der
Rheinischen Friedrich-Wilhelms-Universität Bonn

vorgelegt von

Johannes Philipp Grün

geboren in Bremen

Bonn, Dezember 2023

Angefertigt mit Genehmigung der Mathematisch-Naturwissenschaftlichen Fakultät
der Rheinischen Friedrich-Wilhelms-Universität Bonn

1. Gutachter: Prof. Dr. Thomas Schultz
2. Gutachter: Prof. Dr. Martin Reuter

Tag der mündlichen Prüfung: 20. März 2024
Erscheinungsjahr: 2024

Abstract

Johannes Philipp Grün

Uncertainty Reduction in Diffusion Magnetic Resonance Imaging Tractography

Diffusion Magnetic Resonance Imaging (dMRI) is currently the only non-invasive method capable of mapping the geometry and microstructure of major white matter tracts in vivo. This technique measures the movement of water molecules along magnetic field gradients. Since fiber tracts impede water movement perpendicular while facilitating it along their length, dMRI can measure intricate microstructural information.

Tractography, the process of reconstructing streamlines representing fiber path bundles, has become indispensable in brain studies and surgical planning due to its low risk and high image quality. However, the entire tractography pipeline, from dMRI measurement through pre-processing to final tractography, is highly susceptible to uncertainties, stemming from complex measurement schemes and model imperfections.

In this work, we study multiple sources of uncertainty in tractography and propose models to mitigate these challenges.

Within our first contribution, model uncertainties, stemming from the necessary choice of an appropriate model a-priori, and measurement uncertainties are examined. Further, the interaction between both types of uncertainties is investigated and novel methods to reduce them are introduced. It is shown that reducing model uncertainty also reduces the susceptibility to measurement noise. Finally, the impact of both methods to tractography is discussed and it is visually demonstrated that both methods increase the completeness compared to a more restrictive model selection approach, while at the same time reducing false positives, compared to the low-rank approach. Quantitative analysis over several subjects from the Human Connectome Project (HCP) and a variety of tracts supports the visual impression.

Within our second contribution, we introduce two novel regularized tractography methods to stabilize the tractography against errors in the local direction field, which are amplified if not taken into account. The first method computes a joint low-rank approximation by considering the local neighborhood, while the second employs an unscented Kalman Filter (UKF) to update the local configuration in each step, based on previous estimations.

The approaches are evaluated on several datasets, such as a high quality dataset from the HCP, a challenge dataset for tractography and a clinical dataset from a tumor patient. Results show that both regularization techniques lead to a significant improvement of reconstruction quality, compared to their unregularized counterparts, Pareto optimal results on the challenge dataset, and also high quality reconstructions within measurements of a tumor patient.

However, the low-rank UKF model, while effectively regularizing, occasionally misses some parts of fanning tracts. This originates in the low-rank model, which is able to recover fiber crossings but lags in accounting for fanning. Within our third contribution, we have combined the Bingham distribution, which is able to capture fanning on the sphere, with the low-rank model. Implementing this model involved to overcome several technical challenges. The approach is evaluated on the HCP dataset for a variety of tracts. Results indicate its clear superiority over the previously presented low-rank UKF model in terms of capturing fanning, while maintaining specificity.

Acknowledgements

I wish to acknowledge the assistance and support received from my colleagues, collaborators and friends during the course of this thesis. Special acknowledgment is extended to Prof. Dr. Thomas Schultz for introducing me to this subject and for the valuable discussions that have greatly contributed to my research. Further, I would like to thank Prof. Dr. Martin Reuter for his valuable feedback.

I also thank my former office mate, Shekoufeh, for engaging conversations and for providing necessary distraction.

I also appreciate the support from my girlfriend Henriette over the last few years, including her understanding during late working hours for deadlines and her assistance with proofreading. I thank Lina for her contribution in creating the Figure 2.2.

Finally, I acknowledge the support of my parents throughout my academic pursuits.

Contents

List of Figures

Chapter 1

Introduction

1.1 Motivation

Diffusion Magnetic Resonance Imaging (dMRI) [70, 98] is the only method able to reconstruct the fiber architecture of tissues in vivo without any known harm to the imaged subject. It measures the dephasing of proton spins while a magnetic gradient field is applied along a diffusion-sensitizing direction. When molecules, mainly water, diffuse in the direction of the applied magnetic gradient field, this causes the proton spins to dephase. Thus, diffusion along that gradient direction leads to a measurable signal loss. Within parts of the human brain the movement is not free, due to barriers such as cell membranes, myelin sheaths and microtubules [13]. By these barriers the movement of water is restricted or the displacement is limited, leading to a signal loss, which reflects the underlying tissue structure.

These properties make dMRI an indispensable tool to get a deeper understanding of the human brain without clinical intervention. Currently, it is used to prepare neurosurgeries and for clinical studies [22, 147, 154, 181, 185]. A typical task is to reconstruct the trajectory of a fiber pathway to answer questions about the anatomical connectivity of different brain regions. Therefore, the local direction field is integrated to generate streamlines, which should represent fiber pathways and is commonly termed as tractography.

As dMRI involves the repeated measurement of the whole brain along different gradients, it is highly susceptible to artefacts due to head movements within and in-between measurements. Further, typical imaging artefacts, such as Gibbs ringing, ghosting etc. are present [152]. Although tools to reduce these uncertainties are available and should be applied, later processing steps should account for inadequacies.

The presented work investigates different sources of uncertainty, namely model uncertainty, measurement uncertainty, and Partial Volume Effect (PVE) uncertainty, which denotes the presence of several tissue types within a single voxel due to the large voxel size.

Firstly, the interaction between model uncertainty and measurement uncertainty is analysed and methods to reduce both types of uncertainty are proposed.

Secondly, we propose two techniques to mitigate measurement uncertainties by estimating regularized local directions. Either by incorporating neighborhood information into the estimation or by applying an UKF, which estimates the new local fiber configuration based on the previous estimations.

Thirdly, a novel model to reduce the impact of PVE is introduced. To account for fiber fanning, the low-rank model, which is able to recover crossings but lacks in reconstructing fiber fanning, is extended. Therefore, each local direction is convolved with a Bingham distribution, which is a generalization of the Gaussian distribution to the unit sphere and is able to account for fiber fanning.

In several experiments it has been shown that the proposed works reduce the uncertainty and are therefore very handy for clinical applications, where data quality is not as good as in large studies such as the HCP.

1.2 Publications

This dissertation is based upon the following three publications:

- [59]: "Model Averaging and Bootstrap Consensus Based Uncertainty Reduction in Diffusion MRI Tractography" by Johannes Grün, Gemma van der Voort, and Thomas Schultz in Computer Graphics Forum, Volume 42, Issue 1, Pages: 217-230, Year 2023.
- [57]: "Spatially Regularized Low-Rank Tensor Approximation for Accurate and Fast Tractography" by Johannes Grün, Samuel Gröschel, and Thomas Schultz in NeuroImage, Volume 271, Year 2023.
- [58]: "Anisotropic Fanning Aware Low-Rank Tensor Approximation Based Tractography" by Johannes Grün, Jonah Sieg, and Thomas Schultz, in proceedings of Medical Image Computing and Computer Assisted Invention Society (MICCAI) International Workshop on Computational Diffusion MRI (CDMRI), Year 2023, Accepted for publication.

Additionally, [60]: "Reducing Model Uncertainty in Crossing Fiber Tractography", Johannes Grün, Gemma van der Voort, and Thomas Schultz in proceedings EG Workshop on Visual Computing for Biology and Medicine (VCBM), Year 2021 has been published and extended into [59]. Further, we published [9]: "Detection and Visual Analysis of Pathological Abnormalities in Diffusion Tensor Imaging with an Anomaly Lens" by Marlo Bareth, Samuel Gröschel, Johannes Grün, Pabo Pretzel, and Thomas Schultz in Eurographics Conference on Visualization (EuroVis) Short Papers, Year 2023.

1.3 Related Work

Uncertainties are prevalent throughout the entire dMRI pipeline, encompassing image acquisition, model selection, and parameter setting of the chosen model.

This section offers a concise, though not exhaustive, overview of various uncertainty sources and some tractography design decisions aimed at mitigating their impact. Schultz et al. provided a broader overview of uncertainties and strategies for a more reliable interpretation of results [139].

During image acquisition, uncertainties arise from both physical and numerical insufficiencies:

Eddy currents, induced by rapidly changing magnetic fields, lead to additional magnetic fields. These fields slightly alter the expected resonance frequency, resulting in image distortions. They can also cause ghosting artifacts, typically overlaying the brain image several times. Such artifacts may also originate from coil heating, patient movements, and errors in the magnetic fields.

Gibbs ringing is occurring near anatomical boundaries due to truncation in the inverse Fourier transformation [51].

Beyond these technical limitations, the measured object itself can introduce uncertainties. This includes within-volume motion, leading to zigzag patterns in the reconstructed image, or between-volumes motion, causing misalignments between different gradient directions or leading to dropout [87]. These examples highlight just a few of the potential errors in a typical dMRI experiment.

In addition to structural noise, random background noise arises from imperfections or limitations of the coils, electronics, and inductive losses in the imaged subject.

While a variety of methods exists to reduce and suppress these measurement uncertainties, all subsequent reconstruction steps should account for these uncertainties. A more detailed list, including recent developments to suppress these uncertainties, has been published by Tax et al. [152].

Within each voxel, a local model is applied to reconstruct the local fiber configuration. In this work, Constrained Spherical Deconvolution (CSD) with a low-rank approximation is the chosen local model [4, 137]. This model offers a mathematically elegant solution to the inverse problem and shows higher angular resolution than other approaches. However, this model is not without uncertainties. For single-shell measurements, it is not possible to estimate PVE, which denotes the existence of several tissue types within one voxel. In a study from 2014 it was estimated that this effect is present in 35-50% of white matter voxels, leading to misalignment of extracted directions and an increase in spurious directions [126]. Multi-shell measurements enable the model to account for PVE and effectively reduce this uncertainty. Further, the assumption that a single response function is valid within the whole brain might be overly simplistic, due to structural differences within the brain. Additionally, while the low-rank model can extract multiple fibers from a fiber distribution function, the number of fibers must be pre-determined. Setting this number too low causes the tractography algorithm to miss relevant directions, while setting it too high introduces spurious directions. Lastly, the low-rank model is a crossing model but unable to recover fiber fanning, which occurs as a result of PVE.

To quantify the impact of noise on parameter estimation of local models, several works have proposed to use bootstrapping. One of the first works by Derek Jones used two acquired dMRI of the same subject and created random bootstraps by selecting randomly from both measurements with replacement [75]. Later, wild bootstrapping was proposed to overcome the necessity of acquiring the same image several times, without loss of performance [77, 177].

To this end, we present a work that employs a Bayesian Framework to estimate the most probable number of fibers within a single voxel and develop a novel average model, which fuses information from all single estimations into one average fiber direction estimation. Further, we use wild bootstrapping to simulate measurement uncertainties and suppress them by building a consensus model through all bootstraps.

Given the extraordinary amount of uncertainties, the reconstruction of streamlines is error-prone, and a vast array of different approaches has been developed to incorporate anatomical priors, such as smoothness or maximum angle assumptions, into the tractography algorithm. The earliest approaches used the diffusion tensor model, capable of reconstructing only a single direction of anisotropy, and applied simple Euler integration to it [11]. This approach suffers from all the aforementioned uncertainties and the model's inability to account for complex fiber geometry within a single voxel. From this point, development split into local and global approaches.

Local approaches are extended to higher order integration schemes to capture higher curvature accurately, considered different models, and used probabilistic fiber direction selection to visualize uncertainty [14, 42]. Moreover, various studies incorporated neighborhood information to derive asymmetric information from the data [46]. Additionally, some works proposed methods to regularize tractography, either by applying a Kalman Filter to allow for the evolution of the current solution [53, 101, 102, 123] or by representing the streamline as a smooth curve with restricted curvature and finding a solution for a local neighborhood [7]. These approaches are helpful to reduce the amplification of single small errors, which would possibly result in a false streamline.

Within our second contribution we propose, two methods to regularize tractography. Firstly, the UKF is extended to work with the low-rank model. Secondly, it is shown that the computation of the joint low-rank approximation is as complex as the computation of a low-rank approximation for a single voxel. This is used to create a joint low-rank approximation, which regularizes over a neighborhood.

As discussed previously, the low-rank model is unable to recover fanning from the fiber Orientation Distribution Function (fODF). Within our third contribution the model is extended to capture fanning. The newly proposed model uses a Bingham distribution to capture fanning along with the fiber direction. This model is combined with the UKF.

Beside the local models, some works have proposed to reconstruct streamlines globally. This should reduce amplification of small errors from local estimations effectively. Commonly, these models minimize a sum of internal energy, i.e., fit to the underlying local model, and some anatomical priors, such as the angle between sections [28, 103, 124].

While these global methods effectively reduce uncertainty through noise, their application is quite limited due to excessive computational requirements, as stated in [124]. Another uncertainty within tractography arises due to the presence of fanning, kissing or bending of fibers within a single voxel. Global models are able to resolve fanning and kissing to some extent, but not entirely [124]. A way to completely resolve this is to set up hard boundary conditions based on prior knowledge.

Such boundary conditions could be the explicit start and end points of a streamline. Several geodesic, i.e., shortest path algorithms, have been proposed [65, 132]. Although these methods effectively resolve the problems of kissing and crossing, determining the true boundary conditions is quite challenging, and incorrect settings can lead to biased results [124].

In recent years, various deep learning-based approaches have been introduced [45, 112, 128, 171]. They offer an effective toolbox to include prior information into tractography and have shown promising results.

For the local model, several methods have been proposed as post-processing steps to overcome limitations such as the inability to differentiate between fanning, kissing and bending. The commonly used SIFT approach filters the streamlines such that the distribution of streamlines within a voxel agrees with the underlying fODF [144, 145]. Another approach, named COMMIT, introduces anatomical priors into the optimization [36, 129].

While these advanced tractography algorithms reduce the impact of data ambiguities, such as fiber kissing, crossing, and bending, they introduce a new set of challenges, namely setting tractography parameters. The most common parameters are seed points, step width, maximal angular deviation, and stopping criteria. Several works have illuminated the impact of these parameters on the final tractogram and have developed visualization tools [19, 25].

1.4 Outline

In Chapter 2, the foundational concepts relevant to this thesis are presented. The mathematical frameworks of tensors and spherical harmonics, along with their interconnections, are introduced in Sections 2.1 and 2.2. Essential aspects of the human brain, crucial for understanding the content of this thesis, are discussed in Section 2.3. DMRI and the mathematical models used to quantify diffusion are the focus of Section 2.4. Section 2.5 sheds light on the key design choices in local fiber tracking. The extension of Kalman Filters to non-linear applications is explored in Section 2.6.

Additionally, Section 2.7 delves into the adaptations of the Gaussian distribution for spherical applications.

Chapter 3 details the primary contributions of this work. An evaluation of model and measurement uncertainties within the low-rank model is presented in Section 3.1, along with a mathematical model designed to mitigate these uncertainties. Two novel approaches for tractography regularization are proposed in Section 3.2. The first method enhances the low-rank approximation by integrating spatial neighborhood data into local fiber configuration estimations. The second method utilizes an UKF to estimate local fiber directions based on previous estimations. Both methods show promising results in various test scenarios. An extension of the low-rank model to account for anisotropic fanning is discussed in Section 3.3.

Finally, Chapter 4 offers an evaluation of these contributions, providing insights into the appropriate application of each approach. This chapter also contemplates the broader implications of this work and further directions of research.

Chapter 2

Background

2.1 Tensors

In this thesis, the foundational concepts of tensor calculus play a pivotal role, particularly as they intersect with spherical harmonics. To ensure clarity and provide context for the subsequent discussions, we present a brief introduction to these essential mathematical constructs.

This introduction covers the necessary main concepts of tensors and is based on the textbook by Fischer [47].

2.1.1 Definitions

Definition 1 *A vector space V over a field $\mathbb{K} \in \{\mathbb{R}, \mathbb{C}\}$ is an abelian group $(V, +)$ equipped with a scalar multiplication operation*

$$\cdot : \mathbb{K} \times V \to V \tag{2.1}$$

$$(\lambda, v) \mapsto \lambda v \tag{2.2}$$

which is distributive and $1 \cdot v = v$ for all $v \in V$ and 1 the identity in $\mathbb{K}$.

Definition 2 *A mapping $\langle \cdot, \cdot \rangle : V \times V \to \mathbb{K}$ with*

- *Conjugate symmetric: $\langle x, y \rangle = \overline{\langle y, x \rangle}$ for $x, y \in V$*
- *Linear: $\langle ax + by, z \rangle = a\langle x, z \rangle + b\langle y, z \rangle$ for $x, y, z \in V$ and $a, b \in \mathbb{K}$*
- *Positive-definiteness: $\langle x, x \rangle > 0$ for $x \in V \setminus \{0\}$*

is called scalar product.

Definition 3 *Given a vector space V over a field $\mathbb{K}$ the set of all linear maps $f : V \to \mathbb{K}$ is called dual space $V^\star$.*

Definition 4 *A covariant tensor $\mathbf{T} \in \mathcal{T}^d = \underbrace{V^\star \otimes \cdots \otimes V^\star}_{d}$ of order d is a multi-linear map $\mathbf{T} : V \times \cdots \times V \to \mathbb{R}$.*

A tensor in $\mathcal{T}^d$ can be expressed in a basis given by $\left(\mathbf{e}_{i_d}^\star \otimes \cdots \otimes \mathbf{e}_{i_d}^\star\right)$ for $i_1, \ldots, i_d \subset \{1, \ldots, n\}$ via

$$\mathbf{T} = \sum_{i_1,\ldots,i_d}^{n} T_{i_1,\ldots,i_d} \mathbf{e}_{i_1}^\star \otimes \cdots \otimes \mathbf{e}_{i_d}^\star, \tag{2.3}$$

where the coefficients $T_{i_1,\ldots,i_d}$ form a d-dimensional array. To evaluate the tensor at a specific point $\mathbf{v}_1, \ldots, \mathbf{v}_d$, we use

$$\mathbf{T}(\mathbf{v}_1, \ldots, \mathbf{v}_d) = \sum_{i_1,\ldots i_d=1}^{n} T_{i_1,\ldots,i_d} v_{1,i_1} \ldots v_{d,i_d}, \tag{2.4}$$

using that $\left(\mathbf{e}_{i_1}^\star \otimes \cdots \otimes \mathbf{e}_{i_d}^\star\right)(\mathbf{v}_1, \ldots, \mathbf{v}_d) = \prod_{k=1}^{d} v_{k,i_k}$.

Definition 5 *A tensor is called symmetric if*

$$\mathbf{T}(\mathbf{v}_1, \ldots, \mathbf{v}_d) = \mathbf{T}\left(\mathbf{v}_{\sigma(1)}, \ldots, \mathbf{v}_{\sigma(d)}\right), \tag{2.5}$$

for any permutation $\sigma \in S(d)$. The space of all symmetric tensors of order d is denoted as $Sym_{n,d}$.

Hence, a symmetric tensor is fully determined by its components with $T_{i_1,\ldots,i_d}$ with $i \leq \cdots \leq i_d$, since all other components can be recovered by $T_{i_1,\ldots,i_d} = T_{i_{\sigma(1)},\ldots,i_{\sigma(d)}}$ and the dimension of $\mathrm{Sym}_{n,d}$ coincides with collecting d balls from a set of n elements: $\binom{n+d-1}{d}$.

2.1.2 Approximation

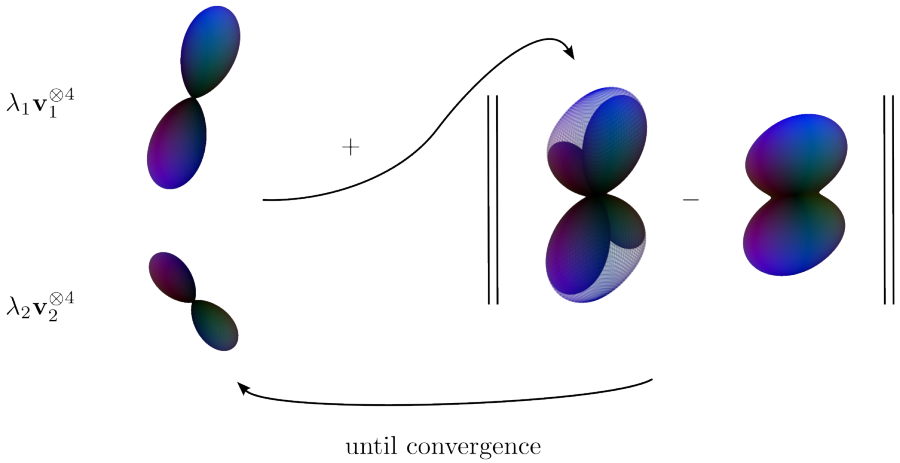

FIGURE 2.1: Schematic representation of the approximation. Left the estimated parameters $\lambda_i, \mathbf{v}_i$, $i = \{1, 2\}$ and right the minimization problem, i.e. norm of the sum of both rank-1 tensors depicted as overlay minus the high order tensor. Now the parameters get optimized until the norm is minimized.

For a real symmetric matrix $M \in \mathbb{R}^{n\times n}$ the spectral theorem[1] states that

$$M = \sum_{i=0}^{n} \lambda_i \mathbf{v}_i \otimes \mathbf{v}_i, \tag{2.6}$$

where $\lambda_i \in \mathbb{R}_{\geq 0}$ and $\mathbf{v}_i \in \mathbb{S}^2$, which denotes the two dimensional sphere. There are algorithms to calculate the rank-r approximation, which include the r greatest eigenvalues.

In general, a symmetric tensor $\mathcal{T}$ of order l can be decomposed into a sum of l-folded rank-1 tensors:

$$\mathcal{T} = \sum_{i} \lambda_i \mathbf{v}_i^{\otimes l}, \tag{2.7}$$

where $\lambda_i \in \mathbb{R}$, $\mathbf{v}_i \in \mathbb{S}^2$ and $\mathbf{v}^{\otimes l} = \underbrace{\mathbf{v} \otimes \cdots \otimes \mathbf{v}}_{l-\text{times}}$. This is commonly referred as low-rank approximation and is in general a hard problem. Within this work, a greedy algorithm is applied, which optimizes the parameters iteratively over the r low-rank tensors, i.e. the objective function gets altered to

$$f\left(\lambda_j, \mathbf{v}_j\right) = \|\mathcal{R}_j - \lambda_j \mathbf{v}_j^{\otimes l}\|_F, \tag{2.8}$$

where $\mathcal{R}_j$ is the residual regarding all other low-rank tensors beside j and $\|\cdot\|_F$ denotes the Frobenius norm. As in the work [57], it can be shown that

$$\lambda_j = \mathcal{R}_j\left(\mathbf{v}_j\right). \tag{2.9}$$

For parameter optimization, a gradient descent algorithm with Armijo step size control is used [6]. Figure 2.1 depicts the approximation.

2.2 Spherical Harmonics

2.2.1 Definitions

A common way to parameterize functions on the sphere is the use of polar coordinates:

$$r : \left(\mathbb{R}_{\geq 0}, [0, \pi], [0, 2\pi)\right) \to \mathbb{R}^3 \tag{2.10}$$

$$(r, \theta, \phi) \mapsto r \begin{pmatrix} \sin(\theta)\cos(\phi) \\ \sin(\theta)\sin(\phi) \\ \cos(\theta) \end{pmatrix}. \tag{2.11}$$

[1] A proof can be found in Fischer, Lineare Algebra, Diagonalisierungssatz [47]

Setting $r = 1$ leads to the unit sphere $\mathbb{S}^2$ and the square integrable functions form an inner product space with inner product

$$\langle f, g \rangle_{\mathbb{S}^2} \coloneqq \int_{\mathbb{S}^2} f \overline{g} d\mu = \int_0^{\pi} \int_0^{2\pi} f(\theta, \phi) \overline{g(\theta, \phi)} \sin(\theta) \, d\phi d\theta. \tag{2.12}$$

A commonly used basis on the sphere are the spherical harmonics, which appear as a solution of the Laplace equation $\Delta f = 0$, when enforcing separability of variables:

Definition 6 *The complex spherical harmonics are the set of functions*

$$\mathcal{Y}_l^m(\theta, \phi) \coloneqq \sqrt{\frac{2l+1}{4\pi} \frac{(l-m)!}{(l+m)!}} P_l^m(\cos(\theta)) \exp(im\phi), \tag{2.13}$$

for $(l, m) \in \mathbb{N} \times \mathbb{Z}$ with $-l \leq m \leq l$ and P_l^m denote the associated Legendre polynomials.

A derivation can be found in [32]. Similarly, the real spherical harmonics can be constructed:

Definition 7 *The real Spherical Harmonics (SH) are defined as*

$$Y_l^m \coloneqq \begin{cases} \sqrt{2} Re\left(\mathcal{Y}_l^{-m}\right) & m < 0 \\ \mathcal{Y}_l^0 & m = 0 \\ \sqrt{2} Im\left(\mathcal{Y}_l^m\right) & m > 0, \end{cases} \tag{2.14}$$

where Im denotes the imaginary part and Re denotes the real part.

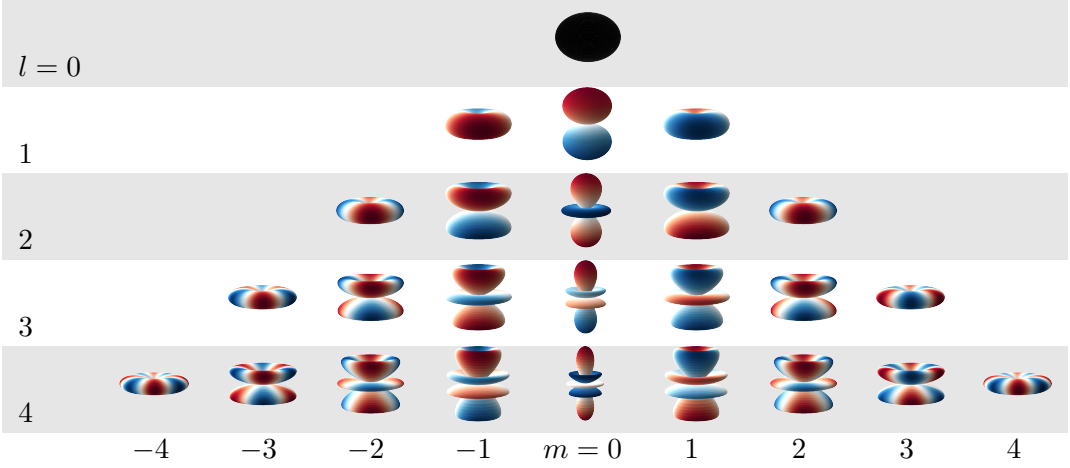

TABLE 2.1: Visualization of the complex spherical harmonics $\mathcal{Y}_m^l$ up to degree $l \leq 4$. The hue represents the complex phase and the radius is scaled by the absolute value.

2.2.2 Properties

Due to the construction, spherical harmonics come with a range of useful properties. In the following subsections the most important ones will be introduced.

Orthonormality and Basis

Due to the normalization constant, the spherical harmonics are orthonormal

$$\langle \mathcal{Y}_l^m, \mathcal{Y}_{l'}^{m'} \rangle_{\mathbb{S}^2} = \langle Y_l^m, Y_{l'}^{m'} \rangle_{\mathbb{S}^2} = \delta_{m,m'} \delta_{l,l'} \text{ for all } |m| \leq l \text{ and } |m'| \leq l' \tag{2.15}$$

and are complete in the square integrable functions on the sphere and thus build a basis.

Expansion

Hence, any square integrable function $f : \mathbb{S}^2 \to \mathbb{C}$ can be expanded as linear combination of this basis, i.e.

$$f(\theta, \phi) = \sum_{l=0}^{\infty} \sum_{m=-l}^{l} f_l^m \mathcal{Y}_l^m(\theta, \phi) \tag{2.16}$$

for coefficients $f_l^m \in \mathbb{C}$. The convergence holds in L^2 and the coefficients can be calculated as

$$f_l^m = \langle f, \overline{\mathcal{Y}}_l^m \rangle_{\mathbb{S}^2}, \tag{2.17}$$

where $\overline{\mathcal{Y}}_l^m$ is the complex conjugated. In a similar way we can calculate the real valued coefficients, using the real valued basis.

Symmetry

Spherical harmonics with even degree l are symmetric and antisymmetric for odd degree:

$$\mathcal{Y}_l^m(-\mathbf{x}) = (-1)^l \mathcal{Y}_l^m(\mathbf{x}). \tag{2.18}$$

Connection between Real and Complex Spherical Harmonics

When a real-valued function f on the sphere is considered, it can be represented in the complex spherical harmonic basis. However, a challenge arises: even though the function itself maps to $\mathbb{R}$, the coefficients f_m^l associated with it might be found to be complex.

Through symmetry and definitions, the following relationships between the complex and real versions of spherical harmonics can be derived:

$$c_l^0 = a_{l0} \tag{2.19}$$

$$c_l^m = \frac{(a_{lm} - i b_{lm})}{\sqrt{2}}, \tag{2.20}$$

where c_l^m are the complex coefficients and a_{lm}, b_{lm} are the real valued coefficients.

These relations permit a direction conversion between real and complex spherical harmonics.

Rotation

A key feature of complex spherical harmonics is the closure under rotations, i.e. rotation of a spherical harmonic leads to a combination of spherical harmonics of the same degree. This shows that the basis is an irreducible representation of the group $\mathrm{SO}(3)$ of dimension $2(l+1)$ and can be formalized as

$$R(\mathcal{Y}_l^m) = \sum_{m'=-l}^{l} \overline{D_{mm'}^{(l)}(R)} \mathcal{Y}_l^{m'}, \tag{2.21}$$

where $\overline{D_{mm'}^{(l)}(R)}$ denotes the complex conjugated of an element of the Wigner D-matrix for a rotation R. As Green pointed out, the computation of the Wigner D-matrix is computational expensive and might be unstable [55]. A more stable and less expensive way is to express the rotations as ZYZ-Euler rotations, or cheaper as five consecutive rotations, where the expensive Y-Euler rotation is replaced by a 90 degrees X rotation, a Z rotation, and a -90 degree X rotation. This leads to the decomposition

$$R(\alpha, \beta, \gamma) = R_z(\gamma) R_x(\pi/2)^T R_z(\beta) R_x(\pi/2) R_z(\alpha), \tag{2.22}$$

where

$$R_x(\theta) \coloneqq \begin{pmatrix} 1 & 0 & 0 \\ 0 & \cos(\theta) & -\sin(\theta) \\ 0 & \sin(\theta) & \cos(\theta) \end{pmatrix} \tag{2.23}$$

$$R_y(\theta) \coloneqq \begin{pmatrix} \cos(\theta) & 0 & -\sin(\theta) \\ 0 & 1 & 0 \\ \sin(\theta) & 0 & \cos(\theta) \end{pmatrix} \tag{2.24}$$

$$R_z(\theta) \coloneqq \begin{pmatrix} \cos(\theta) & -\sin(\theta) & 0 \\ \sin(\theta) & \cos(\theta) & 0 \\ 0 & 0 & 1 \end{pmatrix}. \tag{2.25}$$

Equivalence to Tensors and Polynomials

A bijection exists between real spherical harmonics and the symmetric tensor basis, as it was shown in [41, 115]. Through a linear transformation coefficients can be converted, where the rank l of a truncated SH basis is equal to the order k of a symmetric tensor.

Convolution

Intuitively, the convolution of a function with a kernel smooths the function by averaging the function with the kernel. This definition can be extended for spherical functions with the small restriction that the kernel k is rotational symmetric and can therefore be written as

$$k(\theta) \coloneqq \sum_l f_l \mathcal{Y}_l^0(\theta, \phi) \tag{2.26}$$

which is symmetric around the z-axis and independent of ϕ. We define the convolution on the set of all possible shifts, which coincides with the rotation group $\mathrm{SO}(3)$. We denote that every function $f : \mathbb{S}^2 \to \mathbb{R}$ can be lifted to $\mathrm{SO}(3)$ by setting $\tilde{f}(R) = f(Re_z)$, where $R \in \mathrm{SO}(3)$.

Definition 8 *The spherical convolution of a function $f : \mathbb{S}^2 \to \mathbb{C}$ with a kernel $k : \mathbb{S}^2 \to \mathbb{C}$ is defined as*

$$(k \star f)(\mathbf{u}) = \int_{SO(3)} k(Re_z) f\left(R^{-1}\mathbf{u}\right) dR, \tag{2.27}$$

integrated with respect to the Haar measure with $\int_{SO(3)} dR = 1$.

Theorem 1 *For an isotropic kernel k the convolution becomes a multiplication of the coefficients*

$$(k \star f)_l^m = \frac{1}{\sqrt{4\pi(2l+1)}} k_l f_l^m. \tag{2.28}$$

A proof can be found in [44]. Since the Haar measure is not assumed to be normalized to 1, the constant differs.

2.3 Brain Anatomy

Within this section a short introduction to the anatomy of the human brain is presented, which will help to understand the applied measurement schemes as well as the models to reconstruct local fiber directions. This section is based on the textbook Anatomy [35]. For more details we refer the interested reader to this book. Figures 2.3-2.5 within this section are adapted from the 20th edition of this book, which was released into public domain and can be found online.

The human brain stands at the epitome of biological intricacy, encompassing an estimate in the order of 10 billion neurons [35]. At their core, neurons form the circuitry of our nervous system. They are essential for encoding information and establishing complex networks through inter-neuronal interactions. These vast numbers of neurons oversee everything in the body, from fundamental physiological functions to complex cognitive tasks.

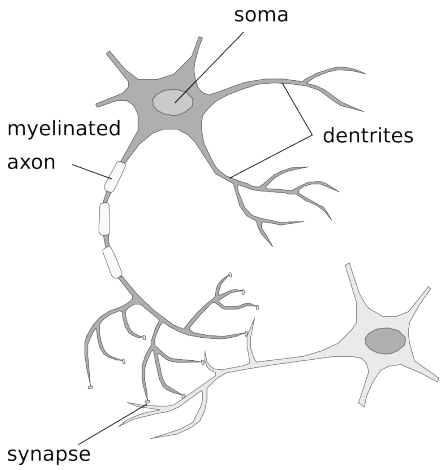

FIGURE 2.2: Simplified representation of neuron with basic synaptic connections.

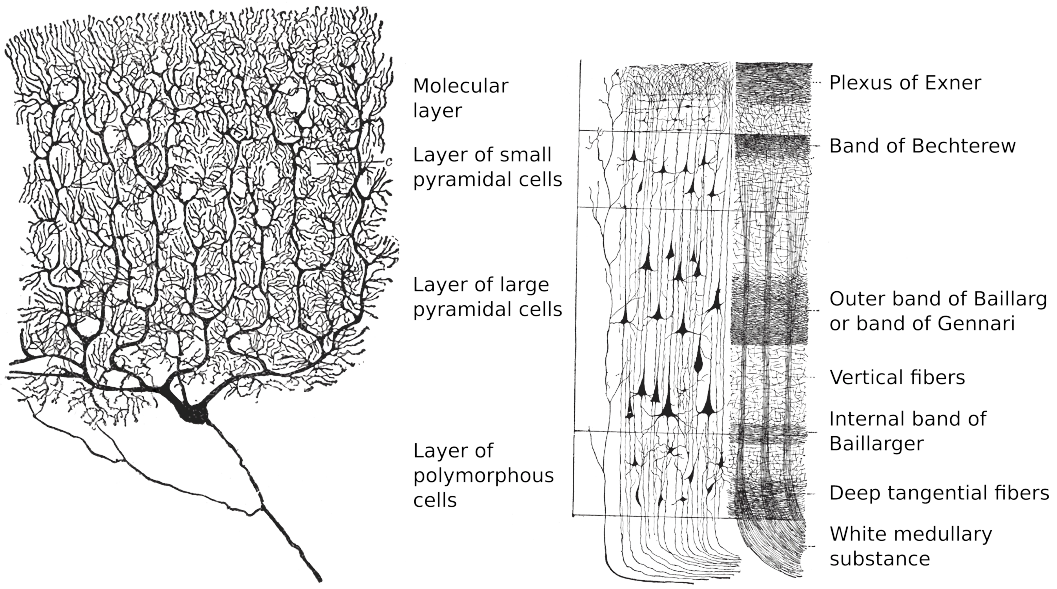

(A) Neuron in the cerebellum with branching dendrites.

(B) Layers in the Gray Matter (GM).

FIGURE 2.3: Example of neuron structures.

A neuron is structured with a soma, or cell body, from which several slender extensions arise. These extensions are categorized as axons, which are primarily responsible for transmitting signals, and dendrites, which predominantly receive them. However, it is worth noting that in certain scenarios, dendrites can also emit signals. The juncture where an axon of one neuron interacts with the dendrite of another is termed a synapses. A schematic representation of neuron is depicted in Figure 2.2 and more complex neuron structures are depicted in Figure 2.3.

The communication between neurons is facilitated through the release of neurotransmitters at the synapses when an axon sends a signal. These neurotransmitters are then taken up by the dendrites, triggering a response in the connected neurons.

While the diameter of an axon typically ranges between 1 and 15μm, their lengths can vary significantly. Many axons are as short as dendrites, but some span much longer distances, connecting regions that are far apart, such as different areas of the brain or even the toe tips to the brain. Long axons are typically enveloped in myelin, a fatty, insulating sheath. This sheath aids in transmitting signals more rapidly. Tissues with high myelin density are termed White Matter (WM), which will be the primary focus of this thesis due to its inclusion of fiber bundles. These bundles consist of groups of well-organized axon structures that connect different regions of the brain.

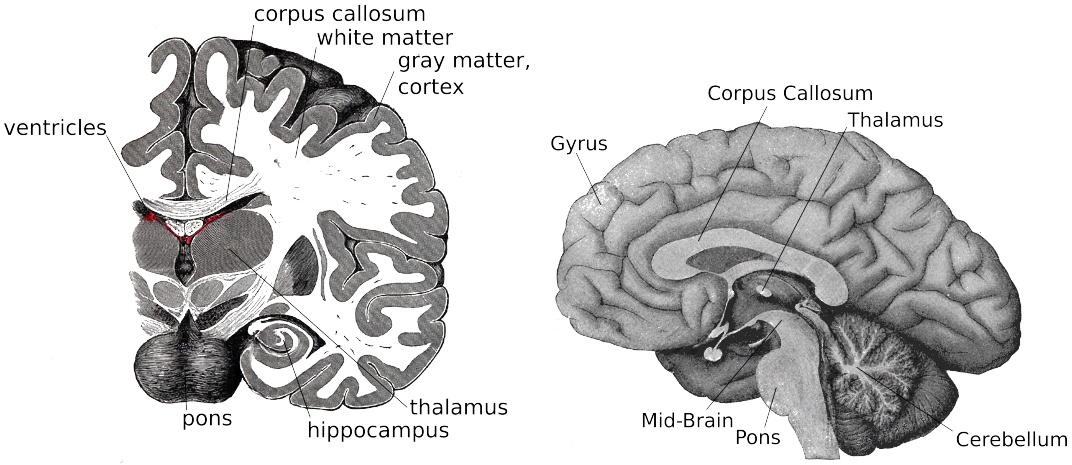

(A) Axial cut through the brain showing WM and Gray Matter (GM).

(B) Sagittal view showing the Corpus Callosum (CC).

FIGURE 2.4: Visualizations of the brain.

In addition to WM, there are two other major tissue types in the brain. One such type is the Cerebrospinal Fluid (CSF), which is housed within the ventricles[2]. This fluid does not contain aligned fiber structures. Additionally, the brain's outer layer, known as the cortex, is composed of Gray Matter (GM). This is a densely packed tissue characterized by short and unorganized connections. Sagittal and axial cuts of the brain are visualized in Figure 2.4.

The bundles can be characterized into three groups. Firstly, association fibers which stay within one hemisphere. Examples which are relevant in this work are the Inferior Fronto-Occipital Fasciculus (IFO), the Inferior Longitudinal Fasciculus (ILF), and the Superior Longitudinal Fasciculus (SLF). Secondly, commissural fibers which connect both hemispheres. The Corpus Callosum (CC) is one example for commissural fibers. Thirdly, projection fibers which connect the cerebral cortex with other parts of the brain. An example is the Corticospinal Tract (CST). Figure 2.5 visualizes some association fibers.

In the subsequent sections dMRI will be introduced, which is capable to measure the diffusion of water in the brain.

[2]Being precise, CSF is not a tissue since it contains fluid. However, in context of MRI it is commonly denoted as tissue, as by Zhang et al. [188]

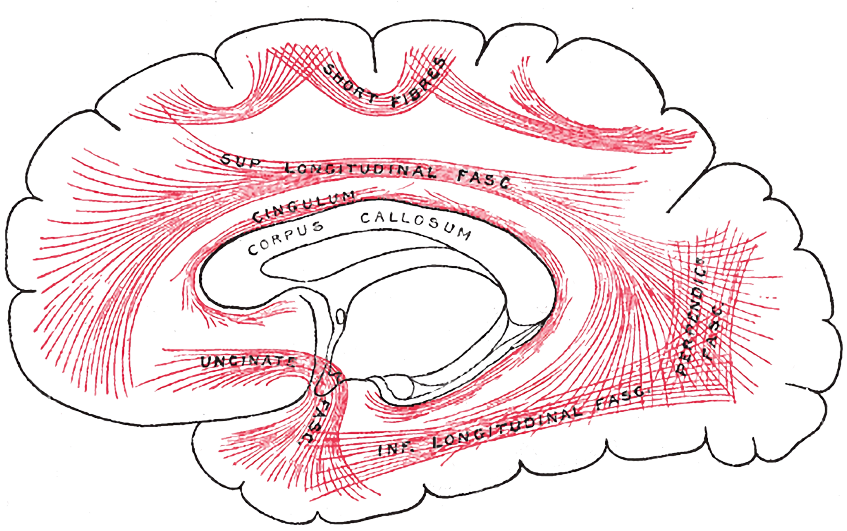

FIGURE 2.5: Sagittal cut showing different association fibers (red) in the white matter.

DMRI has a resolution of approximately 1 mm isotropic, which is far below the resolution of a single axon, but due to strong alignment of fibers within WM, structures are visible.

2.4 Diffusion Magnetic Resonance Imaging

Diffusion Magnetic Resonance Imaging (dMRI) employs a specific Magnetic Resonance Imaging (MRI) sequence that utilizes the diffusion of water molecules as a contrast agent [10]. This allows for unique, in vivo, and non-invasive insights into the human brain. The diffusion process within tissues is not random; instead, it reflects interactions with structures, such as fibers. As a result, diffusion measurements can unveil intricate details of brain structure without posing any known risk to the patient. The subsequent subsections will provide a brief overview of the basic concepts of MRI and dMRI. This chapter is based on the textbook by Brown [21], which contains a more detailed description.

2.4.1 Magnetic Resonance Imaging

The foundational principle behind MRI is Nuclear Magnetic Resonance (NMR), which was discovered around 1940 by Felix Bloch and Edward Purcell. Both received a Nobel Prize in 1952 for their work.

MRI leverages the interaction between nuclear magnetic moments of particles and an external magnetic field. In MRI, the dominant nucleus is the proton in hydrogen, found for example in water molecules. This accounts for two-thirds of the atoms in the human body [68]. Protons constantly spin around their own axis, acting as small magnets [56]. This behavior is formalized with a spin-vector $\mathbf{s}$ of length $\|\mathbf{s}\| = \frac{\sqrt{3}}{2}\hbar$ and a magnetic moment $\mu = \gamma\mathbf{s}$.

Here, $\hbar \approx 1.0546 \cdot 10^{-34}$Js is the reduced Planck constant, and $\gamma \approx 267.5 \cdot 10^6 \frac{\text{rad}}{\text{sT}}$ is the gyromagnetic ratio of protons. In the absence of an external magnetic field, these axes are randomly distributed, canceling each other out and leading to a zero net magnetization $M = \frac{1}{V}\sum_i \mu_i = 0$ in the volume V. When an external magnetic field B_0 is applied, the axes of the proton align in its direction and rotate around the axis of B_0 with the Larmor frequency $\omega = \gamma B_0$. The magnetic moments are either aligned parallel or anti-parallel to the B_0 field with a slightly larger fraction aligned with the field leading to a measurable magnetization M_0 aligned with B_0.

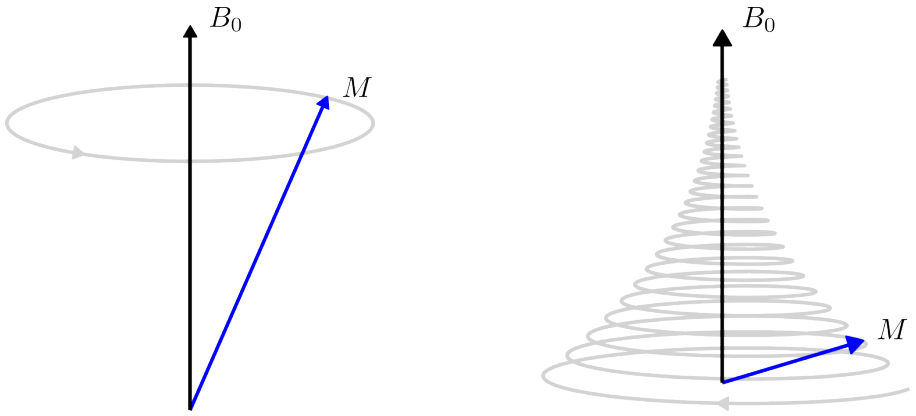

(A) Magnetization M precesses around an applied field B_0.

(B) Relaxation effects as described by the Bloch Equation (2.29).

FIGURE 2.6: Effect of relaxation to the magnetization M. Gray lines describe the trajectory of the magnetization.

To generate a measurable signal, a second magnetic field B_1, perpendicular to B_0, is applied. For simplicity, we assume that B_0 is aligned with the z-axis. The B_1 field is a short pulsed Radio Frequency (RF) at ω rotating in the x-y plane. This leads to a coherent rotation of the spins, yielding to a net magnetization precessing with ω. Shortly after such a pulse, the excited transversal magnetization continues to rotate, decaying according to T_2-relaxation, due to loss of phase coherence. The T_1 relaxation describes the recovery of the longitudinal magnetization and occurs exponentially. This relaxation is intricate but can be described by the Bloch equation for a z-aligned B_0 field:

$$\frac{dM}{dt} = \gamma M \times B_0 - e_x \frac{M_x}{T_2} - e_y \frac{M_y}{T_2} - e_z \frac{M_z - M_0}{T_1}, \tag{2.29}$$

where T_1 describes the spin-lattice relaxation time, T_2 describes the spin-spin relaxation time, and M_0 represents the initial magnetization. The Bloch equation characterizes the relaxation of the net magnetization as an exponential decay over time. After the RF pulse, the spins produce an oscillating magnetic field, which can be detected by a receiver coil tuned to ω. The signal is called Free Induction Decay (FID) and should decay according to the Bloch Equation with T_2.

However, due to inhomogeneities in the static B_0 field and resulting differences in the Larmor frequency, the FID is always shorter than T_2 and can be written as

$$\frac{1}{T_2^\star} = \frac{1}{T_2} + \frac{1}{T_2'}, \tag{2.30}$$

where T_2' describes the decay introduced by the inhomogeneity of the magnetic field.

Different tissue types have different T_1 and T_2 decays, depending on the free water and density of the tissue [106]. For example, CSF and other liquids have high T_1 and T_2 decay times [56]. In general T_1 relaxation times are about 5-10 times longer than T_2 times [34].

Spin Echo

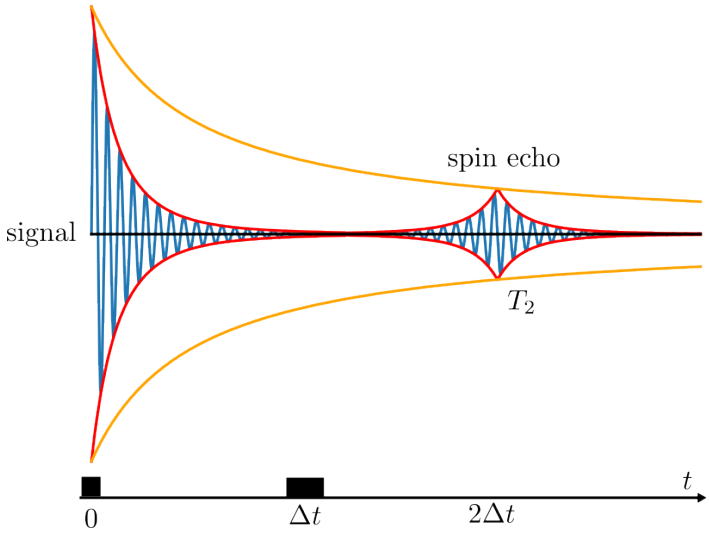

FIGURE 2.7: Application of a spin echo to refocus. At $t = 0$ the initial pulse is applied, at $t = \Delta t$ the pulse is flipped and at $t = 2\Delta t$ the spin echo is present.

As described previously, inhomogeneities in the B_0 field lead to different precession rates of the spins, resulting in FID. To mitigate this effect, a second pulse, flipped by 180°, is applied after time t, following the initial 90° pulse. This pulse inverts the phase of the spins. After a duration of t, the faster spins catch up with the slower ones, and the spins are refocused. This process compensates for the de-phasing caused by inhomogeneities and aids in retaining the signal's clarity and strength.

Spatial Localization

While it is now possible to receive a signal from the protons, achieving spatial resolution is not possible. Instead, we detect an overall signal

$$S = \int_V m\,(x, y, z)\,dV, \tag{2.31}$$

where V represents the volume and m denotes the signal strength at position (x, y, z).

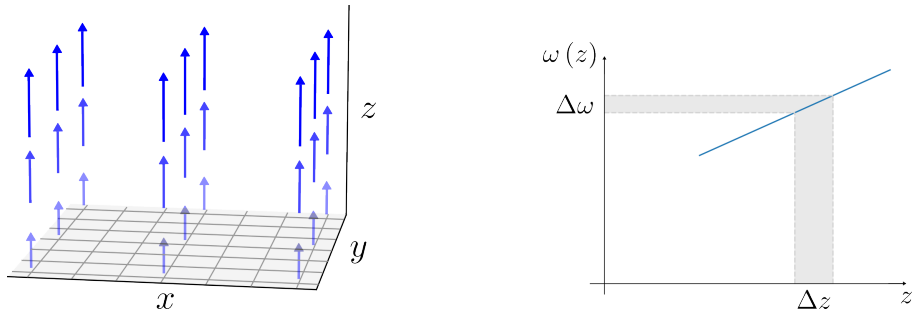

FIGURE 2.8: The applied magnetic field with an additional gradient in the z-direction, yielding to a z dependent Larmor frequency. Hence, a radio pulse will only resonate to a small slice around z.

A common technique to overcome this limitation is by adding a gradient to the B_0 field leading to a varying Larmor frequency along the gradient. Assuming the gradient G_z is in the z direction, the magnetic field becomes $B_0(x, y, z) = B_0 + zG_z$ yielding a Larmor frequency $\omega(x, y, z) = \gamma B_0(x, y, z)$. Using this gradient, it is possible to select a thin slice along the z-axis by tuning the B_1 radio pulse to the corresponding Larmor frequency as depicted in Figure 2.8.

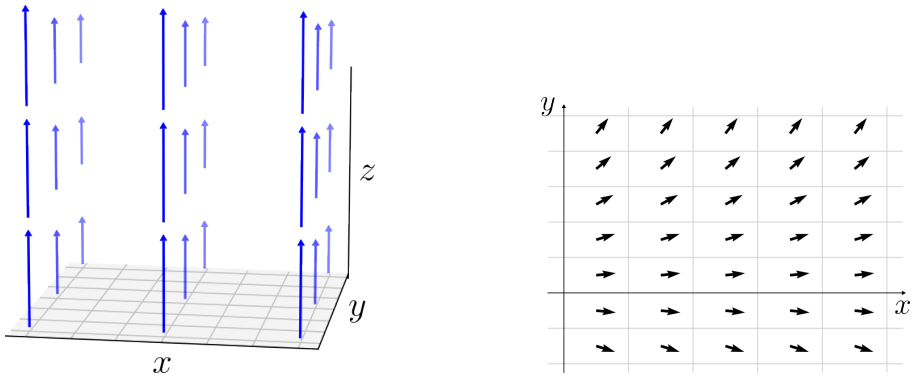

FIGURE 2.9: The phase encoding is carried out by an additional y-gradient applied to B, leading to a change of the rotation frequency $\omega(y)$ during the application and phase differences along the y-axis.

To achieve spatial resolution in the x and y directions, additional techniques are employed. For separability along the x-axis, another gradient, G_x, is applied during the readout time. This results in a varying frequency along the gradient, a process referred to as frequency encoding. By applying a Fourier transformation to the received signal, the signal can be separated based on this frequency variation.

Phase encoding is applied to achieve spatial resolution along the y direction: After the radio pulse, another gradient, G_y, is applied. This causes protons at different y-locations to precess at different speeds. Subsequently, the phase of these protons is shifted in proportion to the strength of the gradient. Figure 2.9 shows how the phase shift leads to different shifts along the y axis and therefore provides information about their position along the y-axis.

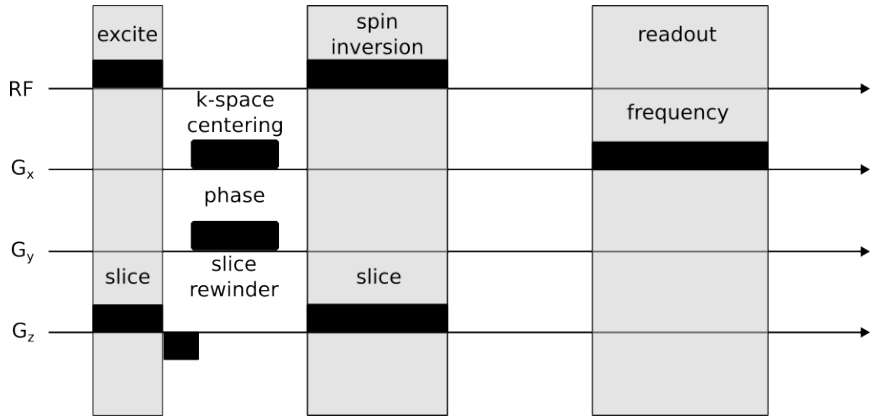

FIGURE 2.10: Schematic spin echo sequence. The RF pulse is applied with additional gradient in z-direction to excite a thin slice. A slice rewinder is applied to reduce phase dispersion of the transverse magnetization. Afterwards the phase encoding along the y axis and k-space centering along the x axis is applied. Then spin inversion is applied to account for inhomogeneities in the magnetic field. During the readout frequency encoding is applied.

By combining these three gradient techniques (slice selection, frequency encoding, and phase encoding), it is possible to determine the spatial position of signals within a 3D volume. A schematic representation of this process is depicted in Figure 2.10.

2.4.2 Diffusion Magnetic Resonance Imaging

DMRI enables the measurement of the diffusion of water molecules by introducing additional gradient pulses. In the absence of any external field, water molecules naturally move around due to their kinetic energy, exhibiting random motion patterns known as Brownian motion. The specific pattern of this diffusion is influenced by the surrounding structures.

For instance, in regions without boundaries, such as the CSF, water molecules move freely in all directions. Their paths are altered primarily by collisions with other molecules, resulting in isotropic diffusion, where the diffusion is uniform in all directions. Conversely, in WM tissues, the cellular structures restrict the movement of water molecules [109]. This confinement causes the molecules to predominantly spread along the direction of the structures and less perpendicular to them, leading to anisotropic diffusion [117].

To harness the diffusion properties of water molecules, Stejskal and Tanner introduced the Pulse Gradient Spin Echo (PGSE) technique [150]. This method employs two consecutive RF pulses: the first pulse is applied at 90 degrees, tipping the net magnetization from its equilibrium position into the transverse plane, and the second pulse is applied at 180 degrees. Surrounding the 180-degree RF pulse, two gradient pulses are applied.

The initial gradient pulse causes de-phasing of the spins. The subsequent 180-degree RF pulse inverts the phase, and the second gradient pulse aims to re-phase the spins. If the molecules remain stationary, the re-phasing aligns the spins since the gradient strength remains consistent. However, if there is diffusion in the gradient direction, molecules experience different gradient strengths during de-phasing and re-phasing. This discrepancy results in a measurable signal reduction due to loss of focus.

Stejskal and Tanner formulated the effect on the spin echo intensity as:

$$S(d) = S_0 \exp(-bd), \tag{2.32}$$

where S_0 is the base signal without applied diffusion gradients, d is the diffusion coefficient along the gradient direction, and the b-value is given by:

$$b = (\gamma G \delta)^2 \left(\Delta - \frac{\delta}{3}\right). \tag{2.33}$$

In this equation, γ represents the gyromagnetic ratio, G is the strength of the applied gradient pulse, δ denotes the pulse duration, and Δ is the time interval between the two gradient pulses.

2.4.3 Diffusion Tensor Imaging

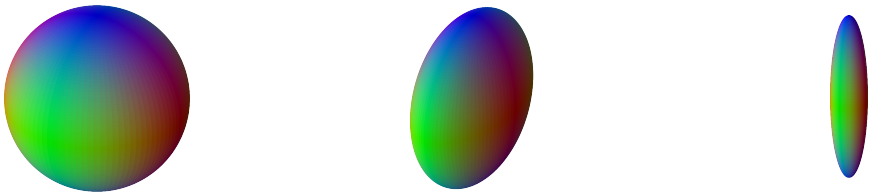

(A) Isotropic tensor with FA = 0.

(B) Anisotropic tensor with equal first and second eigenvalue and FA = 0.33.

(C) Anisotropic tensor with FA = 0.75.

FIGURE 2.11: Visualizations of Diffusion Tensor Imaging (DTI) for different Fractional Anisotropy (FA) values.

By incorporating multiple gradient directions, we can generalize Equation (2.32) to:

$$S(\mathbf{x}) = S_0 \exp\left(-b\mathbf{x}^T \mathbf{D} \mathbf{x}\right), \tag{2.34}$$

where $\mathbf{D} \in \mathbb{R}^{3\times3}$ represents the symmetric diffusion tensor and $\mathbf{x} \in \mathbb{S}^2$. Owing to its symmetry, only six independent components are necessary to fully define the diffusion tensor. In theory, the tensor can be determined using just six diffusion-weighted measurements with non-collinear gradient directions.

However, in clinical practice, more than six measurements are typically acquired to mitigate the effects of noise and enhance the accuracy of the tensor estimation [76]. The parameters are then estimated by computing the least squares fit. This method is commonly named Diffusion Tensor Imaging (DTI).

The diffusion tensor can be decomposed into its eigenvalues, ordered by magnitude, and their corresponding eigenvectors. The primary eigenvector represents the predominant direction of fiber orientation within the voxel. This directionality provides valuable insights into the underlying microstructural organization of the tissue.

For visualization purposes, an ellipsoid can be constructed, with its axes aligned to the eigenvectors of the diffusion tensor. The lengths of these axes are scaled by the corresponding eigenvalues, providing a geometric representation of the diffusion characteristics within the voxel. An example is depicted in Fig. 2.11.

Among the scalar measures, one of the most common is Fractional Anisotropy (FA), which quantifies the anisotropy or directionality of the diffusion within a voxel. It is calculated as:

$$FA = \sqrt{\frac{(\lambda_2 - \lambda_1)^2 + (\lambda_3 - \lambda_2)^2 + (\lambda_1 - \lambda_3)^2}{2\left(\lambda_1^2 + \lambda_2^2 + \lambda_3^2\right)}}, \tag{2.35}$$

where λ_1, λ_2, and λ_3 are the eigenvalues of the diffusion tensor. High FA values are typically found in single fiber WM regions, while low FA values suggest more isotropic diffusion, as seen in GM or CSF or crossing regions.

While the single tensor model is able to capture a primary fiber direction, it falls short when it comes to multi-fiber reconstruction. Considering that 70 to 90% of the WM volume contain multiple fiber orientations, this limitation is significant [72, 133].

A direct extension of the model to account for multiple fibers might look like:

$$S = S_0 \sum_i f_i \exp\left(-b\mathbf{x}^T \mathbf{D}_i \mathbf{x}\right), \tag{2.36}$$

where $\mathbf{x} \in \mathbb{S}^2$, $\mathbf{D}_i \in \mathbb{R}^{3\times3}$ denotes the diffusion tensors and $f_i \in \mathbb{R}_+$ denotes the volume fractions. If the signal is isotropic, i.e. $\mathbf{x}^T\mathbf{D}\mathbf{x} = d \in \mathbb{R}_+$ for all $g \in \mathbb{S}^2$, the extensions leads to ambiguities as the expression can be rewritten as follows:

$$f \exp(d) = f \exp(\underbrace{d_1 + d_2}_{=d}) \tag{2.37}$$

$$= \underbrace{f \exp(d_1)}_{=f_1} \exp(d_2) = f_1 \exp(d_2), \tag{2.38}$$

hence the diffusion tensor and the volume fraction are interchangeable. This problem can be solved by the ball-and-stick model, which models the isotropic part of the measurement as ball and diffusion as sticks [14].

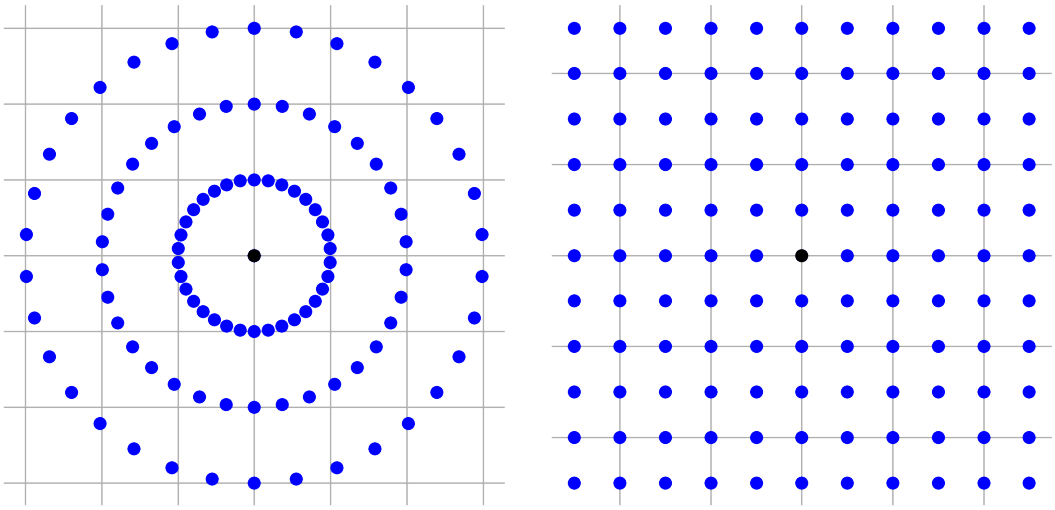

(A) Multi-shell sampling with 3 shells as conducted by the Human Connectome Project.

(B) Cartesian grid sampling.

FIGURE 2.12: Different Q-space sampling schemes illustrated in 2D.

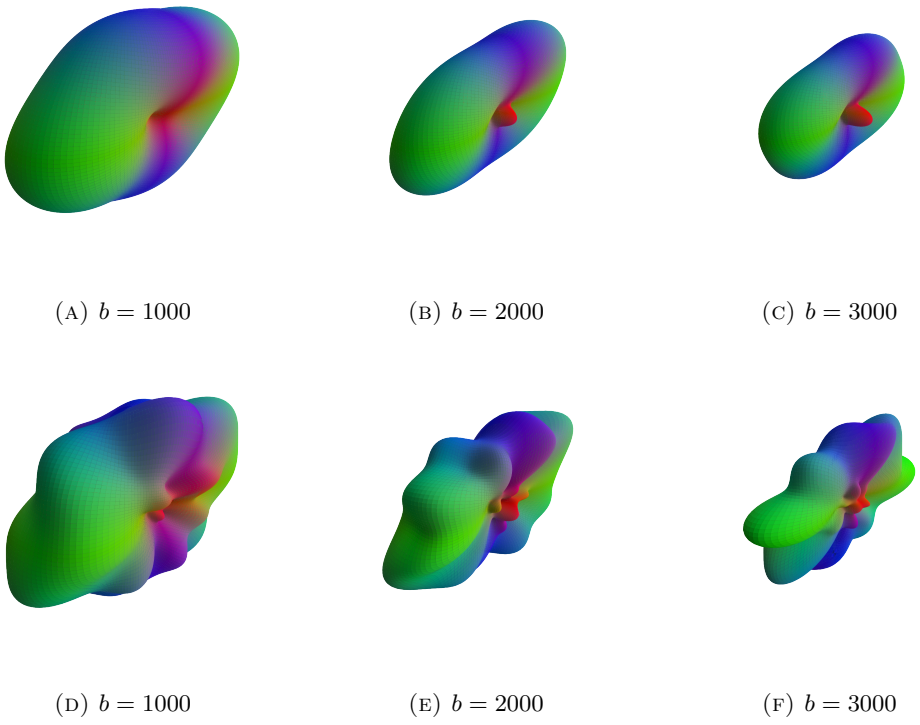

(A) $b = 1000$ (B) $b = 2000$ (C) $b = 3000$

(D) $b = 1000$ (E) $b = 2000$ (F) $b = 3000$

FIGURE 2.13: Visualization of a single voxel measurement from an HCP subject. A least square fit for a fourth (top row) and tenth (bottom row) order spherical harmonics basis is estimated per shell. With increasing b-value the diffusion and therefore the signal loss increases, leading to decreasing signal with increasing b-value. Further, the diffusion profile gets sharper. The surface is color coded by projecting XYZ-axis on RGB colors.

2.4.4 Q-space and Shells

As discussed in the last section, a key challenge is the measurement of $S(g)$, which highly depends on selecting suitable directions $\mathbf{g} \in \mathbb{S}^2$ measured at a b-value. Commonly, these quantities are unified to a b-vector $\mathbf{b} = b\mathbf{g}$ or in so called q-space notation

$$\mathbf{q} = q\mathbf{g}, \text{ with } q = \gamma G \delta. \tag{2.39}$$

As stated before, it is sufficient to measure at seven different directions (including the S_0 measurement). However, to fully approximate the space, it would be ideal to measure at every position. Obviously, this is not possible and a discrete number of directions has to be chosen. The most common measurement schemes are either to sample the q-space on a Cartesian grid, called Diffusion Spectrum Imaging (DSI) [174] or on spherical shells for a few q values, called High Angular Resolution Diffusion Imaging (HARDI) [161]. HARDI requires just a fraction of the sample points DSI is using and is used in the HCP for $b = \{1000, 2000, 3000\}$ $^{\text{mm}}/_{\text{sec}}$ on 90 gradient directions per shell and additional 18 b_0 measurements. Figure 2.13 depicts an example white matter voxel measurement from the Human Connectome Project (HCP). With increasing b-value the signal loss increases and the signal gets sharper.

2.4.5 Deconvolution of dMRI Data

While earlier models were grounded in physical descriptions and delineated a finite number of fiber directions, spherical deconvolution offers a departure from this approach. Instead, it introduces a continuous density function:

$$f : \mathbb{S}^2 \to \mathbb{R} \tag{2.40}$$

$$\mathbf{v} \mapsto f(\mathbf{v}). \tag{2.41}$$

This function is termed the fiber Orientation Distribution Function (fODF). The underlying assumption here is that the diffusion signal can be expressed as a convolution of the fODF with a kernel. This presupposes that all fibers contribute the same MR signal, up to their orientation [159]. The kernel describes the projection of the single fiber response function on a delta peak. Therefore, the single fiber response is represented a convolution between a kernel and a delta peak. We will denote this kernel as delta-kernel.

In this model, a linear mapping is established by utilizing the fact that the convolution of a rotationally symmetric delta-kernel with a spherical harmonic function can be reduced to a matrix multiplication, as detailed in Section 2.2.2. The parameters are then estimated by a linear least squares fit. A notable advantage of this method is that there is no need to predefine the number of fibers, allowing for a more adaptive and accurate representation of the fiber orientations within a voxel [159].

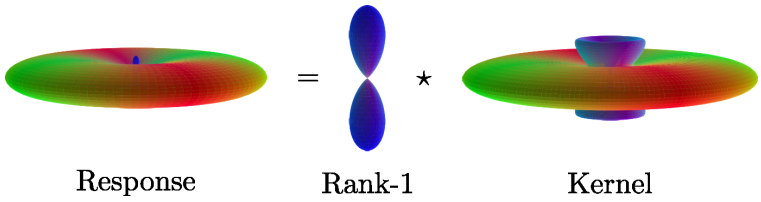

FIGURE 2.14: Left: a single fiber response. Center: Rank-1 kernel as proposed by Schultz and Seidel [137]. Right: the resulting rank-1 kernel.

The single fiber response function is commonly estimated by selecting the $n \in \mathbb{N}$ voxels with the highest FA values within in the brain, aligning them with the z - axis, computing a least squares fit of a spherical harmonic basis model for each voxel and averaging the coefficients. The response function is then extracted as the zonal symmetric part of the series, i.e. Y_l^0 for $l \in \{0, 2, \ldots, 2n\}, n \in \mathbb{N}$ [159]. Figure 2.14 shows an example response function.

Spherical deconvolution of dMRI data often faces challenges due to noise and various artifacts. A notable consequence of these challenges is the emergence of negative values in the resulting fODF. Such negative values are contradictory both to the mathematical model of a distribution function and to the intuitive understanding of fODFs, where negative values do not have a clear physical interpretation.

To address this issue, Tournier et al. introduced Constrained Spherical Deconvolution (CSD). This method iteratively penalizes negative values on a discrete set of directions. The result is a significantly improved fODF representation that contains only minimal negative fractions, aligning better with the expected properties of a distribution function and the inherent nature of fODFs [158].

Due to the large voxel size, many voxels are affected by PVE, i.e. the presence of several tissue types within one voxel [126]. As the signal decay differs between different tissues with increasing b-values, it is possible to differentiate between tissues, such as WM, GM, and CSF, if multi-shell measurements (measurements at different b-values) are available. Therefore, the CSD approach has to be extended to account for multi-shell data. Further, while the approach effectively reduces the occurrence of negative values in the fODF, it does not ensure a strictly positive solution. As a result, there are instances where the resulting fODF might still present non-interpretable negative values.

Jeurissen et al. modeled a distinct response function for each shell and tissue type to account for PVE [74]. This method is practical and effective for a limited number of shells. However, as the number of different b-values grows, the complexity of the approach escalates rapidly. Hence, the method is not applicable to measurement protocols with many distinct b-values, such as DSI.

The constructed delta-kernel faces numerical instabilities, due to the inability of a limited SH basis to represent a delta peak. To enhance the computational stability, Schultz and Seidel have represented the response function as a convolution between a rank-1 peak and a kernel [137].

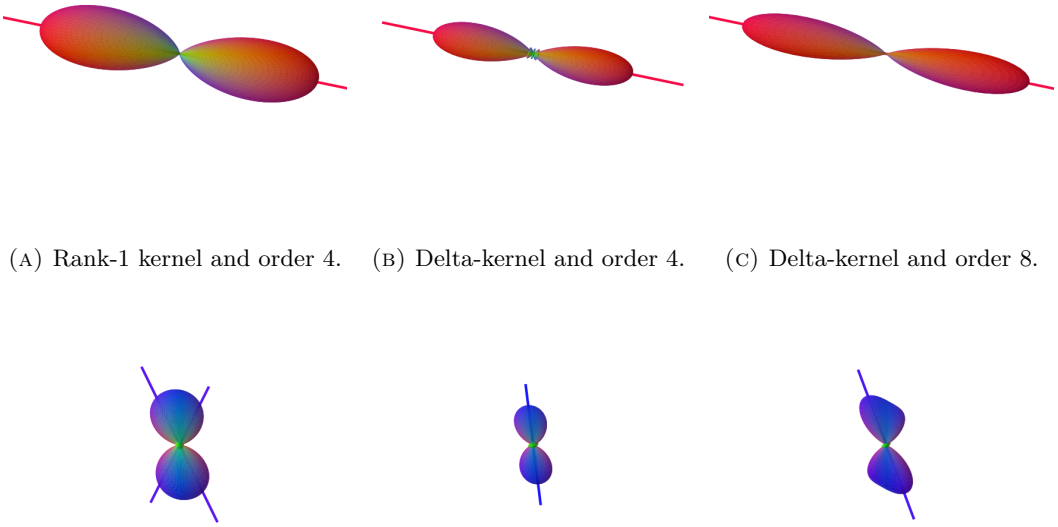

(A) Rank-1 kernel and order 4. (B) Delta-kernel and order 4. (C) Delta-kernel and order 8.

(D) Rank-1 kernel and order 4. (E) Delta-kernel and order 4. (F) Delta-kernel and order 8.

FIGURE 2.15: Top row shows the deconvolution of the signal from Figure 2.13 for all shells. Bottom row shows deconvolution in a crossing fiber region. For Subfigures (A) and (D) the main directions align with the directions from the low-rank approximation, which is depicted as scaled lines in the background. For the remaining subfigures the directions align with the local maxima. With the application of the low-rank approximation it is possible to recover two directions.

In this setup, the fiber directions align with the low-rank approximation of the resulting fODF. While this introduces an additional computational layer, the trade-off is justified by the reduction in angular error.

Ankele et al. tackled the challenges of potential negativity and the limitation to a few b-values by representing the single fiber response in a SHORE basis, which captures the whole spectrum of b-values [4]. In the tensorial framework, non-negativity amounts to a positive semidefiniteness constraint (H-psd) that can be enforced with quadratic cone programming. A visual comparison between the proposed method by Jeurissen et al. and Ankele et al. is depicted in Figure 2.15.

2.5 Tractography

In the previous subsection, we discussed methods to estimate local fiber distributions. A prevalent objective in dMRI research is to piece together entire fibers by logically linking local fiber directions. This process is often termed tractography. There exists a huge variety of tractography algorithms.

Commonly, iterative approaches are used, which are divided into deterministic and probabilistic approaches. A typical deterministic tractography pipeline is composed as follows:

Given local directions, either by a DTI, a low-rank, or any other discrete model, tractography is conducted by defining a seed point with an initial direction and then growing the so-called streamline iteratively by selecting a direction and applying an integration scheme until a stopping criteria is reached.

In each step, a new direction is selected based on the current streamline direction. In case of the low-rank model, the closest peak to the current direction is chosen, in the easier DTI model the present principal eigenvector direction is used. Commonly, easy Euler integration is performed, i.e. taking the direction and following it for a fixed step size [108]. However, also more evolved Runge-Kutta approaches are used, reducing the possible integration error [11].

Common stopping criteria encompass factors like insufficient data support, such as low WM density, exiting the WM, low FA, or notably high curvature.

Deterministic tractography struggles to capture the intricate geometry of the human brain. Specifically, it fails to discern fiber configurations like kissing and fanning. To address this limitation, there is a shift towards probabilistic techniques. For instance, rather than selecting the nearest peak of a fODF, the fODF is interpreted as a probability distribution, and the subsequent direction is determined through random sampling [157]. Alternatively, a probability can be assigned to each discrete fiber direction based on their alignment with the current direction and a random draw determines the next direction. There is a vast array of such strategies, each with its own set of advantages and drawbacks [77]. A shared shortcoming of probabilistic methods is their propensity to produce outliers, and they often lack reproducibility.

For completeness, there are also other tractography approaches, which, instead of using iterative local integration schemes, try to set up a global minimization problem [89]. While they have a few benefits, a great drawback of these methods is the computational infeasibility.

2.6 Filter

In Section 2.1.2, the low-rank r approximation of a high-order tensor was introduced. This approximation serves as a local optimization problem within each voxel to estimate r fiber directions. To refine the streamline estimation, our objective is to introduce a sense of regularity. This can be realized by embedding dependencies among the estimations. A straightforward approach would be to initialize the optimization based on the solution derived from the preceding step and restrict the deviation from the initialization.

Revisiting this problem from a stochastic perspective, we can conceptualize it as a sequence of random variables $(X_t)_{t\in\mathbb{N}}$. These variables represent the state at a given time $t \in \mathbb{N}$, here the set of possible directions.

Moreover, we operate under the assumption that the estimation of current parameters is solely influenced by the previous parameter estimation.

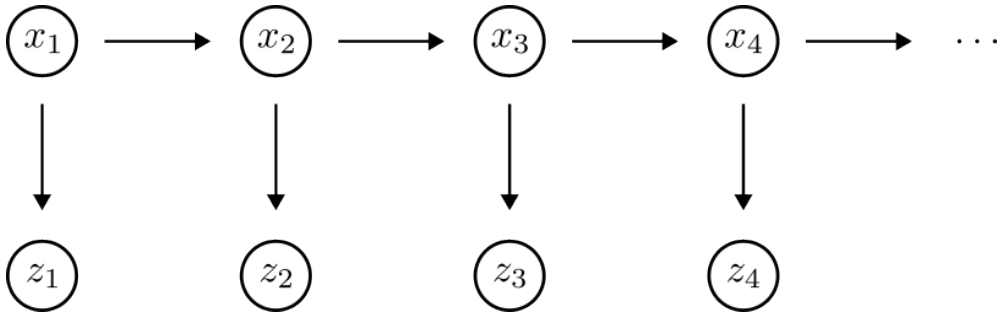

FIGURE 2.16: Schematic representation of a hidden Markov model. The z_i are observables, while x_i are the hidden states of interest.

While the random variables $(X_t)_{t\in\mathbb{N}}$ are not directly observable and are thus termed "hidden", we do observe the measurements $(Z_t)_{t\in\mathbb{N}}$. These measurements are directly linked to the unobserved variables via the low-rank model. The pair $\left((X_t)_{t\in\mathbb{N}}, (Z_t)_{t\in\mathbb{N}}\right)$ is referred to as a hidden Markov model. A representation of this model is depicted in Figure 2.16. At this juncture, this formalization has not provided us with any new insights. The intriguing and logical subsequent query is: Given a sequence of observations, how can we deduce the hidden state? In the realm of statistics, this challenge is commonly known as the filtering problem [8].

In the following subsection, a solution to this problem, namely the Kalman Filter, is introduced. Although the low-rank approximation is non-linear, first the linear problem is considered and afterwards it is extended to the non-linear case. Further, the Kalman Filter is viewed with Bayesian glasses. To prove that the Kalman Filter is a Maximum A Posterior (MAP) estimator, it is assumed that the errors are normally distributed. We denote that Gaussianity of the errors is not necessary to proof the more general minimal mean square error optimally, as pointed out by Uhlmann and Julier [162]. Therefore, it is just assumed that the first two moments of the errors are known.

2.6.1 Kalman Filter

The Gauss Markov model satisfies the following assumptions: The next measurement at time n can be expressed as:

$$Z_n = \mathbf{H}X_n + \varepsilon_n. \tag{2.42}$$

Additionally, the time update is given by:

$$X_n = \mathbf{A}X_{n-1} + \nu_{n-1}, \tag{2.43}$$

where $\mathbf{H}$, $\mathbf{A}$ are linear mappings, X_n is the hidden state, $\varepsilon_n \sim \mathcal{N}(0, \mathbf{R})$, $\nu_n \sim \mathcal{N}(0, \mathbf{Q})$ are mutually independent normal distributed errors and Z_n is the observation.

To get insight into the hidden state, Bayes rule will be the guardian angle, since it allows to link the prior knowledge with the likelihood. The Bayes rule is

$$\mathbb{P}(X \mid Z) = \frac{\mathbb{P}(Z \mid X)\,\mathbb{P}(X)}{\mathbb{P}(Z)}, \tag{2.44}$$

where $\mathbb{P}(Z)$ is the evidence of the marginal likelihood, $\mathbb{P}(X)$ is the prior probability, $\mathbb{P}(X \mid Z)$ is the posterior probability of X given Z, and $\mathbb{P}(Z \mid X)$ is the likelihood. Hence, Bayes rule can be utilized to express our belief about the next step based on past observations.

To apply the Bayes rule to the recursive problem, we calculate the prior belief from Eq. (2.43) yielding $X_n \sim \mathcal{N}\left(\mathbf{A}\mathbf{x}_{n-1}, \mathbf{A}\mathbf{P}_{n-1}\mathbf{A}^T + \mathbf{Q}\right)$, where $\mathbf{P}_{n-1}$ denotes the covariance of X_{n-1}.

Derivation of the Update Equations

Given our model, we aim to compute the MAP estimator to estimate the most likely next state. Ignoring the denominator from Bayes rule, the MAP estimator becomes

$$\begin{aligned}
\arg\max_{\mathbf{x}_n} \mathbb{P}(X_n \mid Z_n) &= \arg\max_{\mathbf{x}_n} \mathbb{P}(Z_n \mid X_n)\,\mathbb{P}(X_n) && (2.45)\\
&= \arg\min_{\mathbf{x}_n} \left(\mathbf{z}_n - \mathbf{H}\mathbf{x}_n\right)^T \mathbf{R}^{-1} \left(\mathbf{z}_n - \mathbf{H}\mathbf{x}_n\right) && (2.46)\\
&\qquad + \left(\mathbf{x}_n - \mathbf{A}\mathbf{x}_{n-1}\right)^T \left(\mathbf{A}\mathbf{P}_{n-1}\mathbf{A}^T + \mathbf{Q}\right)^{-1}\\
&\qquad \cdot \left(\mathbf{x}_n - \mathbf{A}\mathbf{x}_{n-1}\right).
\end{aligned}$$

This formulation captures the trade-off between fitting the observation and staying close to the model's prediction. Further, it shows the impact of noise which acts as a regularizing parameter in this sum.

As a next step, the equation is differentiated regarding $\mathbf{x}_n$ and rearranged, such that $\mathbf{x}_n$ is separated. Together with

$$\mathbf{x}_{n|n-1} = \mathbf{A}\mathbf{x}_{n-1} \tag{2.47}$$

$$\mathbf{P}_{n|n-1} = \mathbf{A}\mathbf{P}_{n-1}\mathbf{A}^T + \mathbf{Q} \tag{2.48}$$

this yields:

$$\begin{aligned}
\mathbf{x}_n &= \left(\mathbf{H}^T\mathbf{R}\mathbf{H} + \mathbf{P}_{n|n-1}^T\right)^{-1} \left(\mathbf{H}^T\mathbf{R}^{-1}\mathbf{z}_n + \mathbf{P}_{n|n-1}^{-1}\mathbf{x}_{n|n-1}\right) && (2.49)\\
&= \left(\mathbf{P}_{n|n-1} - \mathbf{P}_{n|n-1}\mathbf{H}^T \left(\mathbf{R} + \mathbf{H}\mathbf{P}_{n|n-1}\mathbf{H}^T\right)^{-1} \mathbf{H}\mathbf{P}_{n|n-1}\right) && (2.50)\\
&\quad \left(\mathbf{H}^T\mathbf{R}^{-1}\mathbf{z}_n + \mathbf{P}_{n|n-1}^{-1}\mathbf{x}_{n|n-1}\right)\\
&= \mathbf{x}_{n|n-1} + \mathbf{K}_n \left(\mathbf{z}_n - \mathbf{H}\mathbf{x}_{n|n-1}\right), && (2.51)
\end{aligned}$$

with

$$\mathbf{K}_n \coloneqq \mathbf{P}_{n|n-1}\mathbf{H}^T \left(\mathbf{R} + \mathbf{H}\mathbf{P}_{n|n-1}\mathbf{H}^T\right)^{-1}. \tag{2.52}$$

To derive Equation (2.50), the Woodbury matrix identity is used [183]. This allows to update the state in a Bayes optimal way, given the last state and a new measurement. The covariance matrix can be updated by calculating

$$\begin{aligned}
\mathbf{P}_n &= \mathbb{E}\left(\mathbf{x}_n\mathbf{x}_n^T\right) && (2.53)\\
&= \mathbb{E}\left(\left(\mathbf{x}_{n|n-1} + \mathbf{K}_n\mathbf{z}_n - \mathbf{K}_n\mathbf{H}\mathbf{x}_{n|n-1}\right)\right. && (2.54)\\
&\quad \left.\cdot \left(\mathbf{x}_{n|n-1} + \mathbf{K}_n\mathbf{z}_n - \mathbf{K}_n\mathbf{H}\mathbf{x}_{n|n-1}\right)^T\right)\\
&= \mathbf{P}_{n|n-1} - \mathbf{K}_n\mathbf{H}\mathbf{P}_{n|n-1}. && (2.55)
\end{aligned}$$

Applying this scheme leads to MAP optimal estimations of the new state. The Kalman Gain can be simplified to

$$\mathbf{K}_n = \mathbf{P}_{\mathbf{xz}}\mathbf{P}_{\mathbf{zz}}, \tag{2.56}$$

using

$$\begin{aligned}
\mathbf{P}_{n|n-1}\mathbf{H}^T &= \mathbb{E}\left(\left(\mathbf{x}_{n|n-1} - \mathbb{E}\left(\mathbf{x}_{n|n-1}\right)\right)\left(\mathbf{x}_{n|n-1} - \mathbb{E}\left(\mathbf{x}_{n|n-1}\right)\right)^T\right)\mathbf{H}^T && (2.57)\\
&\quad + \mathbb{E}\left(\mathbf{x}_{n|n-1} - \mathbb{E}\left(\mathbf{x}_{n|n-1}\right)\right)\mathbb{E}\left(\varepsilon - \mathbb{E}\left(\varepsilon\right)\right)\\
&= \mathbb{E}\left(\left(\mathbf{x}_{n|n-1} - \mathbb{E}\left(\mathbf{x}_{n|n-1}\right)\right)\right. && (2.58)\\
&\quad \left.\cdot \left(\left(\mathbf{x}_{n|n-1} - \mathbb{E}\left(\mathbf{x}_{n|n-1}\right)\right)^T\mathbf{H}^T + \varepsilon^T - \mathbb{E}\left(\varepsilon^T\right)\right)\right)\\
&= \mathbb{E}\left(\left(\mathbf{x}_{n|n-1} - \mathbb{E}\left(\mathbf{x}_{n|n-1}\right)\right)\right. && (2.59)\\
&\quad \left.\cdot \left(\mathbf{H}\mathbf{x}_{n|n-1} + \varepsilon - \mathbb{E}\left(H\mathbf{x}_{n|n-1} + \varepsilon\right)\right)^T\right)\\
&= \mathbf{P}_{\mathbf{xy}} && (2.60)
\end{aligned}$$

and the fact that $\left(\mathbf{R} + \mathbf{H}\mathbf{P}_{n|n-1}\mathbf{H}^T\right)^{-1}$ is the covariance $\mathbf{P}_{\mathbf{zz}}$ of the observation.

The fundamental assumptions underlying the Kalman Filter are the linearity of the model and the Gaussian nature of the noise and uncertainties. Specifically, the process relies on the fact that the state space follows a Gaussian distribution, and linear transformations preserve this Gaussianity. A general proof can be found in [85].

The Update Equations

To summarize the above, the Equations can be combined to describe one update step of a Kalman Filter as follows: First, the time update is calculated as:

$$\mathbf{x}_{n|n-1} = \mathbf{A}\mathbf{x}_{n-1}, \tag{2.61}$$

$$\mathbf{P}_{n|n-1} = \mathbf{A}\mathbf{P}_{n-1}\mathbf{A}^T + \mathbf{Q}. \tag{2.62}$$

Second, the measurement is updated as:

$$\mathbf{x}_n = \mathbf{x}_{n|n-1} + \mathbf{K}_n \left(\mathbf{z}_n - \mathbf{H}\mathbf{x}_{n|n-1}\right), \tag{2.63}$$

$$\mathbf{P}_n = \mathbf{P}_{n|n-1} - \mathbf{K}_n\mathbf{H}\mathbf{P}_{n|n-1}, \tag{2.64}$$

$$\mathbf{K}_n = \mathbf{P}_{n|n-1}\mathbf{H}^T \left(\mathbf{R} + \mathbf{H}\mathbf{P}_{n|n-1}\mathbf{H}^T\right)^{-1}. \tag{2.65}$$

2.6.2 Extensions to Non-linearity

Since the low-rank r approximation is non-linear, an extension of the traditional Kalman Filter is required. There are two dominant deterministic approaches to address this non-linearity. On the one hand, is the Extended Kalman Filter (EKF). The EKF linearizes the non-linear system using a first-order Taylor series expansion. While it is computationally efficient, its performance can degrade with high non-linearities. On the other hand, the unscented Kalman Filter (UKF) employs a set of deterministically chosen sigma points to capture the mean and covariance of the non-linear transformation. This approach often provides a more accurate representation of the system's true behavior, especially when non-linearities are pronounced [79, 82].

In contrast to the deterministic methods, there is the probabilistic approach of the Particle Filter [39]. This method uses a set of random samples or "particles" to represent the posterior distribution of the state. By propagating these particles through the non-linear system, the particle filter can approximate non-Gaussian and non-linear systems to any order. However, its computational cost is significantly higher than its deterministic counterparts.

Given the need to execute the filtering step millions of times, computational efficiency becomes paramount. While the particle filter offers a high degree of flexibility, its computational demands make it less suitable for applications requiring rapid state estimation. Therefore, deterministic approaches like the UKF are more appropriate. Given the pronounced non-linearities in our model, we opted for the UKF.

2.6.3 Unscented Kalman Filter

As described before, the main achievement of the UKF, is the Unscented Transform, which replaces the non-linear functions with approximations of the density. First we will introduce the new model:

$$Z_n = f(X_n) + \varepsilon_n \tag{2.66}$$

and the time update

$$X_n = h(X_{n-1}) + \nu_{n-1}, \tag{2.67}$$

where Z_n denotes the observation, X_n the unobservable state, h,f some non-linear functions and $\varepsilon_n \sim \mathcal{N}(0, \mathbf{Q})$, $\nu_n \sim \mathcal{N}(0, \mathbf{R})$ Gaussian errors. Given an initial distribution of $X_0 \sim \mathcal{N}(x_0, \mathbf{P}_0)$, we are able to distribute a set of carefully chosen so-called sigma points, which reflect the distribution.

Sigma Points

To fully determine the mean and covariance in dimension n, $n+1$ samples are necessary. That set can be built as described by Julier and Uhlmann [80]. A drawback of this method is that the set is not unskewed in contradiction to a Gaussian distribution. Therefore, we are commonly interested in a set of points, which is also unskewed and has a kurtosis of 3, i.e. is close to Gaussian. Using $2n$ sigma points, the skewness can be easily controlled by distributing them according to the matrix square root. Additionally, a single centered sigma point can be used to control the skewness. Therefore, we use $2n+1$ sigma points, which are trivially distributed as follows:

$$\mathcal{X}_0 = \bar{\mathbf{x}} \qquad w_0 = \frac{\kappa}{n+\kappa} \tag{2.68}$$

$$\mathcal{X}_{i+1} = \bar{\mathbf{x}} + \left(\sqrt{(n+\kappa)\,P_{\mathbf{xx}}}\right)_i \qquad w_{i+1} = \frac{1}{2(n+\kappa)} \tag{2.69}$$

$$\mathcal{X}_{i+n+1} = \bar{\mathbf{x}} - \left(\sqrt{(n+\kappa)\,P_{\mathbf{xx}}}\right)_i \qquad w_{i+n+1} = \frac{1}{2(n+\kappa)}. \tag{2.70}$$

The mean of the sigma points is $\bar{\mathbf{x}}$, the covariance is $\mathbf{P}_{\mathbf{xx}}$, the skewness is zero, since we carefully distributed the points, and the kurtosis depends on κ as follows:

$$\mathbb{E}\left(X^4\right)_j = \sum_{i=0}^{2n+1} \omega_i \left(\mathcal{X}_{i_j}\right)^4 \tag{2.71}$$

$$= \frac{2}{2(n+\kappa)} \left(\sqrt{n+\kappa}\right)^4 \tag{2.72}$$

$$= n + \kappa, \tag{2.73}$$

under the assumption that $\mathbf{P_{xx}} = 1$ and $\bar{\mathbf{x}} = 0$. Since a standard normal distribution has a kurtosis of 3, we can minimize this by setting $n + \kappa = 3$. Negative κ values are possible but might lead to non-positive definiteness of the covariance matrix. If it is assumed that the underlying distribution is non-Gaussian, we can tune the κ parameter differently. Additionally, we note that higher moments of the normal distributed Gaussian follow

$$\mathbb{E}\left(X^l\right) = \begin{cases} 1 \cdot 3 \cdot \ldots \cdot (l-1) & \text{for even } l \\ 0 & \text{else,} \end{cases} \tag{2.74}$$

while the sigma points diverge from this, following

$$\mathbb{E}\left(X^l\right) = \begin{cases} (n+\kappa)^{l/2-1} & \text{for even } l \\ 0 & \text{else.} \end{cases} \tag{2.75}$$

These sigma points are now used to estimate the distribution of the time update and the space mapping as follows:

$$\bar{\mathbf{x}} = \sum_i w_i h\left(\mathcal{X}_i\right), \tag{2.76}$$

$$\mathbf{P_{xx}} = \sum w_i \left(h\left(\mathcal{X}_i\right) - \bar{\mathbf{x}}\right)\left(h\left(\mathcal{X}_i\right) - \bar{\mathbf{x}}\right)^T + \mathbf{Q} \tag{2.77}$$

and

$$\bar{\mathbf{z}} = \sum w_i f\left(h\left(\mathcal{X}_i\right)\right), \tag{2.78}$$

$$\mathbf{P_{zz}} = \sum w_i \left(f\left(h\left(\mathcal{X}_i\right)\right) - \bar{\mathbf{z}}\right)\left(f\left(h\left(\mathcal{X}_i\right)\right) - \bar{\mathbf{x}}\right)^T + \mathbf{R}. \tag{2.79}$$

2.7 Spherical Distributions

Within this section we will introduce two extensions of the Gaussian distribution on the sphere and show important properties. The distributions are used in the presented works to incorporate fiber fanning into the low-rank model by convolving the spherical distribution with a rank-1 peak. The convolution works as described in Section 2.2.2. Therefore a representation in a spherical harmonic basis is necessary. The following Section is based on the textbook by Mardia [104].

2.7.1 Watson Distribution

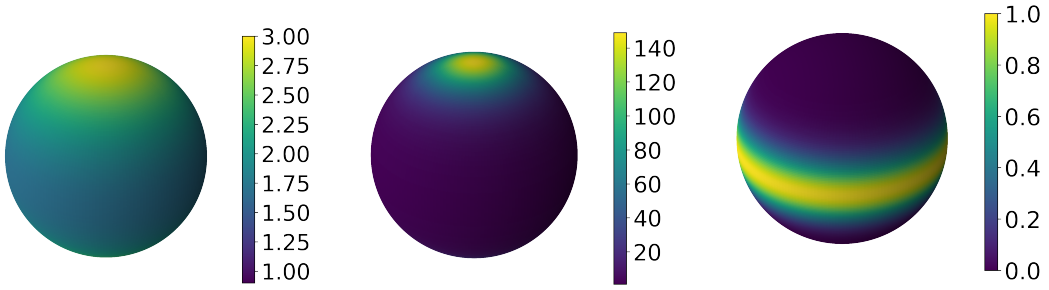

(A) $\kappa = 1$ (B) $\kappa = 5$ (C) $\kappa = -10$

FIGURE 2.17: Watson distribution for different κ values. For increasing values the distribution is more concentrated around its peak. For negative values the distribution is a griddle distribution.

The Watson distribution [172] has the probability density function

$$\begin{aligned} f : \mathbb{S}^2 &\to \mathbb{R}_+ \\ \mathbf{x} &\mapsto \frac{1}{c(\kappa)} \exp\left(\kappa \left(\mu^T \mathbf{x}\right)^2\right), \end{aligned} \tag{2.80}$$

where $\kappa \in \mathbb{R}$ denotes the concentration parameter, $\mu \in \mathbb{S}^2$ the mean direction and the normalization constant $c(\kappa)$ is calculated using the Kummer function as

$$c(\kappa) = 4\pi \cdot {}_1F_1\left(1/2, 3/2, \kappa\right). \tag{2.81}$$

The distribution is rotational symmetric about the principal direction and antipodal symmetric, i.e. $f(\mathbf{x}) = f(-\mathbf{x})$. As seen in Figure 2.17, the concentration depends on the κ parameter: For large κ the concentration around the mean is strong, for $\kappa = 0$ we have a uniform distribution on the sphere and for $\kappa < 0$ we see a symmetric griddle distribution.

Assuming that $\mu = [0, 0, 1]^T$ a series expansion is given by

$$f_{\mathrm{SH}}(\mathbf{x}; \kappa) = \sum_{l=0}^{\infty} c_l(\kappa) \sqrt{\frac{2l+1}{4\pi}} Y_l^0(\theta, \psi) \tag{2.82}$$

where

$$c_l(\kappa) = \begin{cases} 2\pi c(\kappa) \int_{-1}^{1} \exp\left(\kappa t^2\right) P_l(t)\, dt & \text{if } l \text{ even} \\ 0 & \text{else,} \end{cases} \tag{2.83}$$

where $P_n(t)$ is the n-th Legendre polynomial and $c(\kappa)$ is the normalizing constant [64]. Using Mathematica we can evaluate the first coefficients:

$$c_0(\kappa) = 1 \tag{2.84}$$

$$c_2(\kappa) = \frac{1}{4}\left(\frac{3}{\sqrt{\kappa}F(\kappa)} - \frac{3}{\kappa} - 2\right) \tag{2.85}$$

$$c_4(\kappa) = \frac{\frac{5\sqrt{\kappa}(2\kappa-21)}{F(\sqrt{\kappa})} + 12\kappa(\kappa+5) + 105}{32\kappa^2} \tag{2.86}$$

$$c_6(\kappa) = \frac{\frac{21\sqrt{\kappa}(4\kappa(\kappa-5)+165)}{F(\sqrt{\kappa})} - 5\left(8\kappa^3 + 84\kappa^2 + 378\kappa + 693\right)}{128\kappa^3} \tag{2.87}$$

$$c_8(\kappa) = \frac{3\sqrt{\kappa}\left(2\kappa\left(2\kappa\left(62\kappa - 1925\right) + 15015\right) - 225225\right)}{F(\sqrt{\kappa})\,2048\kappa^4} \tag{2.88}$$

$$+ \frac{35\left(8\kappa\left(\kappa\left(2\kappa\left(\kappa+18\right)+297\right)+1287\right)+19305\right)}{2048\kappa^4}. \tag{2.89}$$

2.7.2 Bingham Distribution

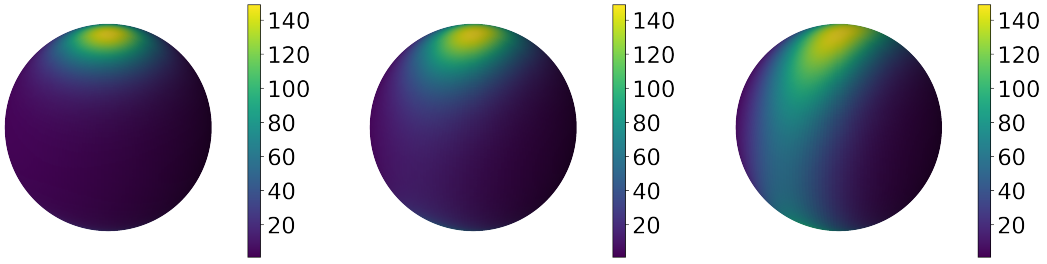

(A) $\kappa = 5$ and $\beta = 0.5$ (B) $\kappa = 5$ and $\beta = 2.5$ (C) $\kappa = 5$ and $\beta = 4$

FIGURE 2.18: Visualization of the Bingham distribution for different β values. For increasing β the distribution becomes more anisotropic.

The Bingham distribution relaxes the rotational symmetric property and has the probability density function

$$\begin{aligned} f : \mathbb{S}^2 &\to \mathbb{R}_+ \\ \mathbf{x} &\mapsto \frac{1}{N(\mathbf{Z})} \exp\left(\mathbf{x}^T \mathbf{M}\mathbf{Z}\mathbf{M}^T\mathbf{x}\right), \end{aligned} \tag{2.90}$$

where $\mathbf{Z}$ is a diagonal matrix with non-increasing entries $z_1 \geq z_2 \geq z_3$, $\mathbf{M} = (\mu_1, \mu_2, \mu_3)$ is an orthogonal matrix and $N(\mathbf{Z})$ denotes the hypergeometric function of matrix argument [17]. Without loss of generality, we set $z_3 = 0$ and rewrite the density function as

$$f(\mathbf{x}; \mu_1, \mu_2, \kappa, \beta) = \frac{1}{N(\kappa, \beta)} \exp\left(\kappa\left(\mu_1^T\mathbf{x}\right)^2 + \beta\left(\mu_2^T\mathbf{x}\right)^2\right), \tag{2.91}$$

where $\kappa = z_1$ and $\beta = z_2$.

Defining the Bingham distribution in this way, μ_1 defines the mean direction, κ its concentration and μ_2 the direction of ellipticity and β the strength. Setting $\beta = 0$ leads to the Watson distribution. While the Watson distribution has a closed form spherical harmonic representation, the Bingham distribution does not provide such an easy solution. But a spherical harmonic representation can be computed numerically for a set of κ and β values with μ_1 aligned to the north pole, since the rotation can be applied afterwards, as discussed in Section 2.2.2.

Chapter 3

Contributions

3.1 Model Averaging and Bootstrap Consensus Based Uncertainty Reduction in Diffusion MRI Tractography

Johannes Grün, Gemma van der Voort, and Thomas Schultz in Computer Graphics Forum, Volume 42, Issue 1, Pages: 217-230, Year 2023.

This study addresses two primary uncertainties in the tractography process and investigates the interactions between them.

Firstly, we address model uncertainty, which arises when estimating the fiber directions within each voxel using the low-rank approximation, since the rank, i.e. the number of fibers, has to be set a priori. Determining the correct number of fibers is pivotal. Setting it too low will overlook fiber directions, while setting it too high will introduce spurious directions. In the first case, the tractography algorithm will miss important parts of the tract, while in the second case, it will find non-existing connections.

To address this problem, the probability of a specific rank, given a fODF is of interest. Bayes rule is applied to connect the posterior probability of the hypothesis that the rank is r given the fODF, with the likelihood of the fODF given that the rank is r, multiplied by the prior knowledge of the rank distribution. Due to inconsistent values in literature, the prior is set as non-informative, i.e., uniform over the ranks. The likelihood is approximated using the Bayesian Information Criterion. It remains essential to calculate or approximate the probability of a fODF given the rank and its parameters, namely fiber directions and lengths. Ideally, a fODF should have a high probability if the approximation error is low and vice versa. This is modeled using a flexible Kumaraswamy Probability Density Function. Instead of selecting the low-rank model with the maximum posteriori probability, it is proposed to create an **average model**. This model fuses fiber direction estimations from all different low-rank r approximations, by first clustering the directions into three groups, ensuring that the distance within groups is minimized and each low-rank r approximations contributes to each group at most once. Each low-rank r contribution is weighted by its posterior probability, ensuring a more accurate and comprehensive representation.

The second uncertainty relates to measurement noise. Due to the complex nature of the dMRI protocol, measurement noise is always present and has multiple sources, such as inhomogeneous magnetic fields, body movement etc.

To quantify and address this, we employ a wild bootstrapping approach. By simulating multiple fODF datasets, we can estimate inherent data uncertainty without additional measurements. Similar to the average model, a **consensus bootstrap model** is constructed, by first matching the fiber directions and afterwards averaging them. While finding global minima for the average model is feasible, due to its limited number of single low-rank models, this becomes challenging for the consensus model. Therefore, an optimization problem is constructed and iteratively the groups are built, such that the distances within the group are minimized and each low-rank model contributes to each group once.

Our findings indicate a strong agreement between the dominant rank in the bootstraps and the most probable rank determined by the Bayesian framework, further endorsing the Bayesian approach.

For each bootstrap realization a **selection model**, i.e. selecting the most probable model by the posterior probability, and an average model are built. Fitting a Watson distribution to the different models, it is evident that both models reduce variability of the main fiber direction compared to a rank-3 model. This shows that both the selection and the average model effectively reduce susceptibility to measurement noise.

Finally, we conduct tractography on 12 subjects from the HCP dataset for 7 tracts, for which reference tractographies are available. We select a single seeding slice and post-processed the tractography results using inclusion and exclusion regions.

A visual comparison of the right CST shows that the consensus model increases the reconstruction density compared to the base models in all cases. It is important to note that the average model is more favourable than the rank-3 model, as it reduces the false positives. To evaluate the reconstructions quantitatively, we compare the results by computing the dice scores, where the reference reconstructions are set as ground truth. It is evident that the median of all models improves with the application of the consensus model. Moreover, a median dice improvement is observed for the average model compared to the selection model. To delve deeper into the results, we conduct a non-parametric Friedman test, revealing significant differences between the dice scores of the models. A Nemenyi post-hoc test identified significant differences, showing that the average and rank-3 consensus model yield significant difference to their respective base models in terms of dice score with a higher mean dice. Further, model averaging shows significant differences compared to the selection model and the rank-3 model with a higher median dice score.

In conclusion, we have investigated two sources of uncertainty, i.e. model uncertainty and measurement uncertainty, and their interaction with each other. It has been shown that the average model successfully reduces both types with much less effort than the bootstrap models.

The main author has contributed the methodology, implementation, validation, data curation, the original draft and all visualizations.

3.2 Spatially Regularized Low-Rank Tensor Approximation for Accurate and Fast Tractography

Johannes Grün, Samuel Gröschel, and Thomas Schultz in NeuroImage, Volume 271, Year 2023.

In recent years, the field of multi-fiber tractography has witnessed significant advancements, with a primary focus on extracting more detailed information from data. Historically, the diffusion tensor imaging model was employed to estimate a single direction of anisotropy. Modern advancements, however, such as the ball-and-stick model, facilitate the reconstruction of multiple fibers. Even more advanced methods, such as CSD, are capable of reconstructing an entire fODF.

However, with increasing model complexity comes heightened susceptibility to noise and other data-related anomalies. While research data quality has improved, thanks in part to initiatives such as the HCP, real-world clinical scenarios pose unique challenges. Economic constraints often mean that clinical measurements are shorter, making them more susceptible to noise and inconsistencies. Given the iterative nature of most tractography approaches, a single local error can amplify, resulting in inaccurate streamline representations. This highlights the necessity of robust regularization techniques in tractography to ensure model reliability in both research and clinical contexts.

To address this, we propose two novel spatial regularization approaches for the low-rank r approximation:

Firstly, instead of approximating each voxel individually, we consider neighboring voxels in the approximation to reduce outliers. It is shown that the **joint low-rank** approximation over local neighborhood does not increase the optimization complexity compared to the low-rank approximation of a single voxel. Further, a weighting scheme is introduced to keep the tract borders intact, while regularizing at the same time.

Secondly, we apply an UKF, to introduce a relation between the previously unrelated measurements. Further, it offers a balance between measurement fit and deviation from the current state, based on covariances of the additive noises.

To validate the efficacy of these models, we conduct extensive benchmarks against existing models. Our first experiment involves twelve randomly selected subjects from the HCP dataset, focusing on seven major tracts with existing reference tractographies. We emulate clinical data quality by limiting the number of gradient directions to 30 and using a single b-value of 1000. Seeding is performed in a single slice of a tract and the performance of the different methods is evaluated using the dice score. As baseline comparison, the low-rank model and a multi-tensor UKF are used.

A visual comparison of the CST shows that the joint low-rank approximation leads to a denser reconstruction than the low-rank model and the low-rank UKF results in a denser reconstruction than the multi-tensor UKF on both the full and reduced data. Comparing the joint low-rank model with the low-rank UKF shows that the joint low-rank model captures the fanning much better. It is also clearly visible that the novel approaches improve the regularity of the reconstructions.

Further, the quantitative results from the reduced dataset reveal that in six out of seven tracts the joint low-rank model has the highest median dice. To analyze the results further, a Friedman test is conducted, which shows significant differences between the dice scores of the models. A Nemenyi post-hoc test shows that the dice of the joint low-rank model differs significantly from all other models. Further, the low-rank UKF shows significant differences to the traditional low-rank and the multi-tensor UKF with a higher median dice.

Our second experiment utilizes the ISMRM challenge dataset. Here, whole-brain tractography is executed, followed by outlier removal and automated tract segmentation. Results, averaged over the tracts, indicate that both proposed methods achieve Pareto optimal results compared to other competitors, consistently across various WM densities that are used as stopping criteria.

Lastly, we evaluate the regularized approaches on a clinical dataset from a tumor patient. We focus on reconstructing the CST due to its close proximity to the tumor. The results are compared to the widely-used iFOD2 tractography framework by MRtrix. A clinical collaborator analyzed the outcomes, concurring that the results were more coherent and complete, compared to iFOD2.

In conclusion, our research has introduced innovative regularization techniques that promise enhanced accuracy and reliability in multi-fiber tractography, serving both research and clinical applications.

The main author has contributed the methodology, implementation, validation, formal analysis, investigation, data curation, writing of the original draft and visualizations.

3.3 Anisotropic Fanning Aware Low-Rank Tensor Approximation Based Tractography

Johannes Grün, Jonah Sieg, and Thomas Schultz, in proceedings of Medical Image Computing and Computer Assisted Invention Society (MICCAI), International Workshop on Computational Diffusion MRI (CDMRI), Year 2023, Accepted for publication.

Previous research demonstrated that the low-rank UKF outperforms the joint low-rank approximation in whole-brain tractography settings in terms of reaching more overlap, while keeping the overreach limited. Further, the model is much faster compared to the joint low-rank method.

However, in a Region of Interest based setting, it fails to capture portions of the tract when fiber fanning is present, due to the inability of the low-rank approximation to model fanning.

To overcome this limitation, we propose to replace the low-rank model with a novel model that convolves each rank-1 peak with a Bingham distribution, which is called **Bingham UKF**. Instead of determining just three parameters (direction and length), it is necessary to ascertain six parameters. Specifically, a rotation with length accounts for four parameters, and the remaining two parameters define the spread of the Bingham distribution. This new model is combined with the UKF.

The implementation of this model presents three main challenges:

Initialization: A proper initialization is essential, since it reduces the false streamlines due to wrong initialization as well as the initial necessity of state adaption. The direct approach would be to identify parameters that minimize the optimization problem, but this is considerably more complex than estimating the low-rank approximation. Within this work, a novel method to estimate the parameters is introduced. Using the fact that the Hessian of the low-rank problem provides insights into the curvature at a given point, it also provides insights into the presence of fanning at a point. A low curvature in a direction indicates that a slight change of the point into this direction would not change the residual dramatically, i.e. spread in this direction is likely, while a strong curvature indicates a sharp peak and no spread. Calculating the eigenvectors of the Hessian reflects the directions with the largest spread and is used as an initialization of the quaternion rotation. To use the relation between the Hessian and the Bingham parameters, a lookup table is created by computing the Hessian for a wide range of Bingham parameters.

Spherical Harmonics of the Bingham Distribution: No closed-form solution exists to represent the Bingham distribution in spherical harmonics. Therefore, we numerically evaluate the integral for a Bingham distribution oriented towards the north pole across a broad spectrum of coefficients. As discussed in Section 2.2.2, the rotation can be applied afterwards.

Representation of Rotations: While the minimal representation of a rotation can be achieved using Euler angles, they come with challenges like gimbal lock. We address this by employing quaternions. Given their normalized nature, this introduces dependencies within the UKF state, possibly leading to degeneration of the covariance matrix. As a solution, we introduce Modified Rodrigues Parameters, establishing a homeomorphism between $\mathbb{R}^3$ and $\mathbb{S}^3$. We map the quaternions to the north pole and subsequently to $\mathbb{R}^3$. This eliminates the state dependencies. Then, the sigma points are distributed in the lower dimensional space and are pulled back.

We compare our approach to the previously introduced low-rank UKF and a Watson UKF model, which only supports isotropic fanning. Our evaluation involves twelve randomly selected subjects from the HCP dataset and seven major tracts.

We use the manually refined reconstructions provided along the TractSeg paper as a baseline. The directed Hausdorff distance's 95% quantile serves as measurement metric, assessing completeness and excess based on argument order.

Visually, the new method presents a significant improvement in completeness. However, overreach is also increased. It is worth noting that a portion of this overreach is not problematic and could be rectified by expert human intervention or advanced filtering techniques.

When comparing the Hausdorff distances, it is evident that in six out of the seven tracts, the Bingham model's completeness surpasses both the low-rank and Watson models. The excess remains moderate across all methods, with a few exceptions. We conduct Friedman tests at the tract level, revealing significant differences in six out of seven tracts for the completeness metric and four out of seven for the excess metric.

In this study, the low-rank model was expanded to accommodate fiber fanning. Along the way, several technical difficulties were overcome. The findings suggest that the new Bingham model effectively addresses the issue of absent fiber fanning, resulting in significantly denser reconstructions. A small caveat is that the time consumption has increased compared to the low-rank UKF and that the evaluation was just performed on high quality data.

The main author has contributed to the methodology, formalization, implementation, data curation, conducting the experiments, and all visualizations.

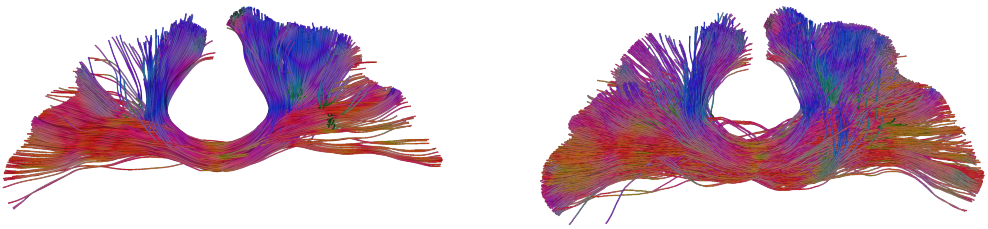

(A) Low-rank UKF (B) Bingham UKF

FIGURE 3.1: Reconstruction of a part of the CC tract in clinical data. The Bingham UKF reconstructs to a larger extent than the low-rank UKF but the streamlines are less organized.

After the submission we have evaluated the Bingham UKF further, with a focus on clinical data. We will present a short visual comparison of a healthy volunteer as addendum.

The dMRI dataset has a resolution of $1.71875 \times 1.71875 \times 1.7$ mm on $128 \times 128 \times 72$ voxels measured at $b = 3000^{\text{s}}/_{\text{mm}^2}$ on 60 directions. Additionally, 6 $b = 0$ volumes are measured. As pre-processing steps, the measurements are denoised using the scripts provided by MRtrix [31, 160], Gibbs ringing is removed [86], and distortion is corrected using topup and eddy_correct [3]. From the corrected data fODFs of order 6 are estimated [4]. The Bingham UKF parameters are adjusted slightly to account for the worse data quality compared to the HCP dataset, i.e. $R = 0.1$.

Seeding is conducted within the center of Corpus Callosum (CC) and exclusion regions are defined to remove outliers. In Figure 3.1 results are depicted. As expected, the low-rank UKF produces more aligned results compared to the Bingham UKF. Therefore, the Bingham UKF is able to reconstruct parts of the fanning, which the low-rank UKF does not reach.

We conclude that the Bingham UKF is applicable to high quality clinical single shell measurements and the reconstruction captures the fanning better than the low-rank UKF. Further experiments on clinical data with lower b-value have to be conducted to determine the clinical applicability of the Bingham UKF in a wider context.

Chapter 4

Discussion

In this dissertation, several novel methods have been developed to mitigate uncertainties. Within this section, the approaches are compared and recommendations for the applications are formulated. Further, possible extensions are presented and the general development of dMRI research is discussed.

The first paper explores both model and measurement uncertainty, highlighting a relationship between them. It demonstrates that model averaging is an effective approach to address both types of uncertainty. While the consensus model requires a large number of samples, leading to significant time consumption, the average model is much quicker, making it the preferred method.

The second paper introduces two innovative methods to spatially regularize tractography using a low-rank model. The results suggest that, based on the setup, either the joint low-rank or the low-rank UKF model outperforms the others. Moreover, the low-rank UKF is considerably faster than both the joint low-rank and the multi-tensor UKF methods. The latter is notably slower because the UKF update requires the inversion of covariance matrices. In the measurement space, the covariance dimension aligns with the number of gradient directions. However, for the low-rank UKF, it aligns with the number of fODF parameters, i.e., 15 for an order 4 model compared to 90 on a single shell of the full HCP dataset.

The third paper presents the innovative Bingham UKF, addressing the limitations of the earlier low-rank UKF, namely the inability to model fiber fanning. The research indicates that the Bingham model increases completeness compared to the low-rank UKF. However, due to the Bingham model's increased complexity, the fODF order has been raised to 6, resulting in 28 dimensions in the fODF space, leading to a longer computation time.

Collectively, these papers have advanced the state-of-the-art in tractography pipelines. Naturally, one might wonder which model is best suited for specific circumstances. While there is no one-size-fits-all answer, we recommend the following:

For those prioritizing computational efficiency, the low-rank UKF emerges as the top choice, being roughly ten times faster than its counterparts.

For single slice seeding, the joint low-rank model or the Bingham UKF are recommended. Although a direct comparison between these two is lacking, the Bingham UKF uses an order 6 low-rank model, while the joint low-rank model employs order 4. This distinction means that the Bingham UKF demands more flexibility and data.

For whole-brain seeding, we suggest opting for either the low-rank UKF or the Bingham UKF. While the low-rank UKF has its limitations, especially its inability to reconstruct fiber fanning, these are offset when seeding directly into the fiber spread. However, when fiber count is of paramount importance, the Bingham UKF may be the more suitable choice due to its ability to recover spread from a wider area.

Concerning the consensus and average models, we do not recommend building the consensus model. Its time-intensive nature and marginal advantages do not justify its use, especially when compared to the significantly faster average model. Although the average model is more efficient and outperforms the selection model, our preference still leans towards the joint low-rank or UKF models. These models have consistently shown superior results without the added complexity of constructing an average model.

The presented research shows a few loose ends which could be closed:

First, the Bingham UKF approach has only been evaluated on the HCP dataset and a high quality clinical dataset. The effectiveness of this approach on a clinical dataset of lower quality remains an unanswered question. While the low-rank UKF and the joint low- rank approximation have demonstrated their effectiveness on low-quality datasets due to their regularizing power, the Bingham UKF, with its inherent flexibility and use of order 6 tensors, may be more susceptible to noise.

Second, the tractography approaches, especially the Bingham approach, could be enhanced by employing a look-ahead strategy. This method involves not only sampling the current next direction but also taking a step in this direction and sampling again. The resulting probability would be the product of both individual steps. From this distribution, a single step is sampled via rejection sampling and a step in the first direction is taken. Although this method is more costly - necessitating more frequent evaluations of the Kalman Filter at each step - it enables the identification of paths closer to borders and likely ensures more reliable navigation through crossing areas. Additionally, paths could be regularized using parallel transport, as suggested by Aydogan et al. [7]. This adjustment would strongly regularize the taken directions in each integration step, leading to more reliable reconstructions, as shown in the work.

Third, an attempt could be made to mitigate model uncertainty by constructing an average model from three individual Kalman filters for each rank. Furthermore, it would be worthwhile to investigate the behavior of a model if the model rank does not coincide with the intrinsic fODF rank. It is possible that some minor fibers may degenerate if the intrinsic fODF rank is lower than the model rank. If this is the case, it could be interesting to reinitialize the model if certain constraints are fulfilled. Lastly, the impact of the UKF measurement and process noise parameters on the resulting reconstruction has to be evaluated in more detail.

In general, it would be beneficial to have an automated adaption to new datasets depending on spatial resolution and data quality.

Fourth, as the low-rank model shows improved reconstructions compared to iFOD2 by MRtrix3, which was used as training reference for the TractSeg model, the model performance might improve if retrained with improved reference tractographies [170]. But alas, the used reference tractograms are manually cleaned. Therefore, it might be necessary to clean the new reconstructions in the same way to achieve better results.

Fifth, it might be an interesting idea to fuse the low-rank model with a learning model, which predicts the next directions at a given point. The fusion could be achieved by predicting a regularized low-rank problem, where the regularizer penalizes the deviation from the estimated directions by the learning model. Tuning the optimization parameter would allow to either trust the low-rank model or the deep learning model more. A similar approach has been tried for fODF and it has been shown that this leads to a higher accuracy, especially if the data quality is rather low [118].

The advancements in fiber tractography presented in this work have far-reaching implications. Within the last couple of years, new dMRI datasets have been published, such as the Parkinsons Progression Markers Initiative [105]. The goal of this project is the better understanding of Parkinsons, which could result in early diagnosis and more efficient treatment. A common way to predict biomarkers is to build an anatomical network based on tractography results and use this network as input for a graph neural network [33]. Since the data quality is relatively worse, compared to the Human Connectome Project, the application of multi fiber tractography approaches is challenging. The proposed regularized tractography methods could be used to create high quality tractographies for the further analysis. As it was shown by Bastiani et al., the improvement in tractography algorithms has a significant impact on the predictions [12]. With the increased accuracy, more fine grained analysis is possible, leading to higher and more consistent deviations between two control groups.

The future of dMRI research is twofold. On the one hand is the evolution of MRI scanners The Human Connectome Project (HCP) began in 2009, and since then, MRI scanners have seen rapid advancements. The gradient strength has nearly doubled, and the speed of gradient evaluation has tripled. This progress allows for measurements at unprecedented resolutions of 0.76 mm isotropic, which is an improvement by a factor of approximately 4.5 compared to the HCP measurements. The q-space is sampled at 1260 directions. While such a scan requires a lengthy 18 hours, the quality it offers is groundbreaking and promises to pave the way for further research [62].

Another emerging trend in the field is b-tensor imaging [176]. While traditional dMRI measures diffusion along a gradient, the b-tensor method adjusts the applied field during the application along a specific trajectory.

This adjustment aims to distinguish between microscopic diffusion within a voxel, a distinction not achievable with the current setup, as it was pointed out already in early 2000 [156]. With the advent of these new techniques, there is a need for the development of new models. The diffusion tensor can be estimated as before, by making the gradient direction time dependent. Currently this research branch is more directed towards microstructural features of the underlying structures [43, 96].

On the other hand, advancements in computer hardware have enabled the construction and optimization of more complex models. Over the past few years, there has been a noticeable shift towards deep learning tractography approaches [15, 119, 170]. These approaches have yielded promising results, but have not yet become the predominant method. This might be due to uncertainties which arrive with learning based tractography. While there exist ways to visualize data fidelity for tractography based on classical integration approaches, for learning based approaches the interpretation of data fidelity is challenging, since the models are learned.

Another significant challenge is the absence of definitive ground truth tractograms. Some strategies have utilized manually refined tractographies from existing models as a baseline [170]. While this serves as a reasonable starting point, the intricate nature of the data and the sheer volume of streamlines make it virtually impossible for manual curation. Nevertheless, the outcomes have been encouraging.

Further, the approaches are normally trained on healthy humans, which have a much smaller variety than ill patients, which can have a huge variety of artefacts, such as tumors or neurodegenerative illnesses, affecting the underlying microstructure and might lead to wrong results.

For neural network tractography purposes, additional information, like the rough shape of a tract, will be learned during the training, making these approaches more stable against outliers and inherit ambiguities within dMRI. While this is a feature for healthy patients, it might be a problem for non-healthy patients. While the tracts are within certain regions of the brain for healthy adults, for tumor patients this is not necessarily the case, as it was shown in the second paper.

Another prevalent method involves approximating models, such as the CSD, using neural networks [90, 99, 110, 111]. The primary advantage of these methods, aside from increased speed, is their ability to operate on raw data. This bypasses the information loss from extensive pre-processing steps.

Additionally, high-quality data can further push the boundaries of what is achievable. While such data acquisition is not practical in clinical settings due to economic constraints and patient time considerations, it could be instrumental in enhancing deep learning approaches by providing a more accurate ground truth.

In this work we have evaluated different sources of uncertainty and developed novel methods to successfully mitigate the. The methods show promising results and indicate further paths of research to continuously improve tractography.

References

[1] Andrew L. Alexander, Khader M. Hasan, Mariana Lazar, Jay S. Tsuruda, and Dennis L. Parker. "Analysis of Partial Volume Effects in Diffusion-Tensor MRI". In: *Magnetic Resonance in Medicine* 45 (2001), pp. 770–780. DOI: 10.1002/mrm.1105.

[2] Daniel C. Alexander, Gareth. J. Barker, and Simon R. Arridge. "Detection and Modeling of Non-Gaussian Apparent Diffusion Coefficient Profiles in Human Brain Data". In: *Magnetic Resonance in Medicine* 48 (2002), pp. 331–340. DOI: 10.1002/mrm.10209.

[3] Jesper L.R. Andersson, Stefan Skare, and John Ashburner. "How to correct susceptibility distortions in spin-echo echo-planar images: application to diffusion tensor imaging". In: *NeuroImage* 20.2 (2003), pp. 870–888. DOI: 10.1016/S1053-8119(03)00336-7.

[4] Michael Ankele, Lek-Heng Lim, Samuel Groeschel, and Thomas Schultz. "Fast and Accurate Multi-tissue Deconvolution Using SHORE and H-psd Tensors". In: *Medical Image Computing and Computer-Assisted Intervention - MICCAI 2016*. Ed. by Sebastien Ourselin, Leo Joskowicz, Mert R. Sabuncu, Gozde Unal, and William Wells. Cham: Springer International Publishing, 2016, pp. 502–510. DOI: 10.1007/978-3-319-46726-9_58.

[5] Michael Ankele, Lek-Heng Lim, Samuel Groeschel, and Thomas Schultz. "Versatile, Robust, and Efficient Tractography With Constrained Higher-Order Tensor fODFs". In: *Int'l J. of Computer Assisted Radiology and Surgery* 12.8 (2017), pp. 1257–1270. DOI: 10.1007/s11548-017-1593-6.

[6] Larry Armijo. "Minimization of Functions having Lipschitz continuous first partial derivatives". In: *Pacific Journal of Mathematics* 16.1 (1966), pp. 1–3. DOI: pjm/1102995080.

[7] Dogu Baran Aydogan and Yonggang Shi. "Parallel Transport Tractography". en. In: *IEEE Transactions on Medical Imaging* 40.2 (Feb. 2021), pp. 635–647. DOI: 10.1109/TMI.2020.3034038.

[8] Alan Bain and Dan Crisan. *Fundamentals of Stochastic Filtering*. en. Ed. by B. Rozovskiĭ and G. Grimmett. Vol. 60. Stochastic Modelling and Applied Probability. New York, NY: Springer, 2009. DOI: 10.1007/978-0-387-76896-0.

[9] Marlo Bareth, Samuel Gröschel, Johannes Grün, Pablo Pretzel, and Thomas Schultz. "Detection and Visual Analysis of Pathological Abnormalities in Diffusion Tensor Imaging with an Anomaly Lens". In: *Eurographics Conference on Visualization (EuroVis) Short Papers*. 2023. DOI: 10.2312/evs.20231041.

[10] Peter J. Basser, Joseph Mattiello, and Denis Le Bihan. "Estimation of the Effective Self-Diffusion Tensor from the NMR Spin Echo". In: *Journal of Magnetic Resonance, Series B* 103.3 (1994), pp. 247–254. DOI: 10.1006/jmrb.1994.1037.

[11] Peter J. Basser, Sinisa Pajevic, Carlo Pierpaoli, Jeffrey Duda, and Akram Aldroubi. "In Vivo Fiber Tractography Using DT-MRI Data". In: *Magnetic Resonance in Medicine* 44 (2000), pp. 625–632. DOI: 10.1002/1522-2594(200010)44:4<625::aid-mrm17>3.0.co;2-o.

[12] Matteo Bastiani, Nadim Jon Shah, Rainer Goebel, and Alard Roebroeck. "Human cortical connectome reconstruction from diffusion weighted MRI: The effect of tractography algorithm". In: *NeuroImage* 62.3 (2012), pp. 1732–1749. DOI: 10.1016/j.neuroimage.2012.06.002.

[13] Christian Beaulieu. "The basis of anisotropic water diffusion in the nervous system – a technical review". In: *NMR in Biomedicine* 15.7-8 (2002), pp. 435–455. DOI: 10.1002/nbm.782.

[14] Tim E.J. Behrens, Heidi Johansen Berg, Saad. Jbabdi, Matthew F.S. Rushworth, and Mark W. Woolrich. "Probabilistic diffusion tractography with multiple fibre orientations: What can we gain?" In: *NeuroImage* 34.1 (2007), pp. 144–155. DOI: 10.1016/j.neuroimage.2006.09.018.

[15] Itay Benou and Tammy Riklin Raviv. "DeepTract: A Probabilistic Deep Learning Framework for White Matter Fiber Tractography". In: *Medical Image Computing and Computer Assisted Intervention – MICCAI 2019*. Ed. by Dinggang Shen, Tianming Liu, Terry M. Peters, Lawrence H. Staib, Caroline Essert, Sean Zhou, Pew-Thian Yap, and Ali Khan. Cham: Springer International Publishing, 2019, pp. 626–635. DOI: 10.1007/978-3-030-32248-9_70.

[16] Pablo Bernal-Polo and Humberto Martínez-Barberá. "Kalman Filtering for Attitude Estimation with Quaternions and Concepts from Manifold Theory". In: *Sensors* 19.1 (Jan. 2019), p. 149. DOI: 10.3390/s19010149.

[17] Christopher Bingham. "An Antipodally Symmetric Distribution on the Sphere". In: *The Annals of Statistics* 2.6 (1974), pp. 1201–1225. DOI: 10.1214/aos/1176342874.

[18] Ralph Brecheisen, Bram Platel, B. M. ter Haar Romenij, and Anna Vilanova. "Illustrative uncertainty visualization of DTI fiber pathways". In: *The Visual Computer* 29.4 (2013), pp. 297–309. DOI: 10.1007/s00371-012-0733-9.

[19] Ralph Brecheisen, Anna Vilanova, Bram Platel, and B. M. ter Haar Romenij. "Parameter Sensitivity Visualization for DTI Fiber Tracking". In: *IEEE Trans. on Visualization and Computer Graphics* 15.6 (2009), pp. 1441–1448. DOI: 10.1109/TVCG.2009.170.

[20] G. Larry Bretthorst, Christopher D. Kroenke, and Jeffrey J. Neil. "Characterizing Water Diffusion In Fixed Baboon Brain". In: *Bayesian Inference and Maximum Entropy Methods in Science and Engineering*. Ed. by Rainer Fischer, Roland Preuss, and Udo von Toussaint. 2004, pp. 3–15. DOI: 10.1063/1.1835192.

[21] Robert W. Brown, Yu-Chung N. Cheng, E. Mark Haacke, Michael R. Thompson, and Ramesh Venkatesan. *Magnetic Resonance Imaging: Physical principles and sequence design*. John Wiley &; Sons, Inc., 2014. DOI: 10.1002/9781118633953.

[22] Ed Bullmore and Olaf Sporns. "Complex brain networks: graph theoretical analysis of structural and functional systems". In: *Nature Reviews Neuroscience* 10 (2009), pp. 186–198. DOI: 10.1038/nrn2575.

[23] Angelika Bunse-Gerstner, Ralph Byers, and Volker Mehrmann. "Numerical Methods for Simultaneous Diagonalization". In: *SIAM Journal on Matrix Analysis and Applications* 14.4 (1993), pp. 927–949. DOI: 10.1137/0614062.

[24] Paul T. Callaghan, Craig D. Eccles, and Yang Xia. "NMR microscopy of dynamic displacements: k-space and q-space imaging". In: *Journal of Physics E: Scientific Instruments* 21.8 (Aug. 1988), pp. 820–822. DOI: 10.1088/0022-3735/21/8/017.

[25] Maxime Chamberland, Kevin Whittingstall, David Fortin, David Mathieu, and Maxime Descoteaux. "Real-time multi-peak tractography for instantaneous connectivity display". In: *Frontiers in Neuroinformatics* 8 (2014). DOI: 10.3389/fninf.2014.00059.

[26] Zhenrui Chen, Yanmei Tie, Olutayo I. Olubiyi, Fan Zhang, Alireza Mehrtash, Laura Rigolo, Pegah Kahali, Isaiah Norton, Ofer Pasternak, Yogesh Rathi, Alexandra J. Golby, and Lauren J. O'Donnell. "Corticospinal tract modeling for neurosurgical planning by tracking through regions of peritumoral edema and crossing fibers using two-tensor unscented Kalman filter tractography". In: *Int'l J. of Computer Assisted Radiology and Surgergy* 11.8 (2016), pp. 1475–1486. DOI: 10.1007/s11548-015-1344-5.

[27] Guang Cheng, Hesamoddin Salehian, John R Forder, and Baba C Vemuri. "Tractography from HARDI using an intrinsic unscented Kalman filter". In: *IEEE Trans. on Medical Imaging* 34.1 (2015), pp. 298–305. DOI: 10.1109/TMI.2014.2355138.

[28] Daan Christiaens, Marco Reisert, Thijs Dhollander, Stefan Sunaert, Paul Suetens, and Frederik Maes. "Global tractography of multi-shell diffusion-weighted imaging data using a multi-tissue model". en. In: *NeuroImage* 123 (Dec. 2015), pp. 89–101. DOI: 10.1016/j.neuroimage.2015.08.008.

[29] SungWon Chung, Ying Lu, and Roland G. Henry. "Comparison of bootstrap approaches for estimation of uncertainties of DTI parameters". In: *NeuroImage* 33.2 (2006), pp. 531–541. DOI: 10.1016/j.neuroimage.2006.07.001.

[30] Pierre Comon, Gene Golub, Lek-Heng Lim, and Bernard Mourrain. "Symmetric Tensors and Symmetric Tensor Rank". In: *SIAM Journal on Matrix Analysis and Applications* 30.3 (2008), pp. 1254–1279. DOI: 10.1137/060661569.

[31] Lucilio Cordero-Grande, Daan Christiaens, Jana Hutter, Anthony N. Price, and Jo V. Hajnal. "Complex diffusion-weighted image estimation via matrix recovery under general noise models". en. In: *Neuroimage* 200 (Oct. 2019). Publisher: Elsevier, p. 391. DOI: 10.1016/j.neuroimage.2019.06.039.

[32] Rirchard Courant and D. Hilbert. "Special Functions Defined by Eigenvalue Problems". In: *Methods of Mathematical Physics*. John Wiley & Sons, Ltd, 1989. Chap. 7, pp. 466–549. DOI: 10.1002/9783527617210.ch7.

[33] Hejie Cui, Wei Dai, Yanqiao Zhu, Xuan Kan, Antonio Aodong Chen Gu, Joshua Lukemire, Liang Zhan, Lifang He, Ying Guo, and Carl Yang. "BrainGB: A Benchmark for Brain Network Analysis with Graph Neural Networks". en. In: *IEEE Transactions on Medical Imaging* 42.2 (Feb. 2023). arXiv:2204.07054 [cs, q-bio], pp. 493–506. DOI: 10.1109/TMI.2022.3218745.

[34] Stuart Currie, Nigel Hoggard, Ian J. Craven, Marios Hadjivassiliou, and Iain D. Wilkinson. "Understanding MRI: basic MR physics for physicians". eng. In: *Postgraduate Medical Journal* 89.1050 (Apr. 2013), pp. 209–223. DOI: 10.1136/postgradmedj-2012-131342.

[35] Anthony V. D'Antoni. *Gray's Anatomy, the Anatomical Basis of Clinical Practice*. Vol. 29. 2. 2016, pp. 264–265. DOI: 10.1002/ca.22677.

[36] Alessandro Daducci, Alessandro Dal Palù, Alia Lemkaddem, and Jean-Philippe Thiran. "COMMIT: Convex optimization modeling for microstructure informed tractography". eng. In: *IEEE transactions on medical imaging* 34.1 (Jan. 2015), pp. 246–257. DOI: 10.1109/TMI.2014.2352414.

[37] Kyriakos Dalamagkas, Magda Tsintou, Yogesh Rathi, Lauren O'Donnell, Ofer Pasternak, Xue Gong, Anne Zhu, Peter Savadjiev, George Papadimitriou, Marek Kubicki, Edward Yeterian, and Nikos Makris. "Individual variations of the human corticospinal tract and its hand-related motor fibers using diffusion MRI tractography". In: *Brain Imaging and Behavior* 14 (2020), pp. 696–714. DOI: 10.1007/s11682-018-0006-y.

[38] Anders M. Dale, Bruce Fischl, and Martin I. Sereno. "Cortical Surface-Based Analysis: I. Segmentation and Surface Reconstruction". In: *NeuroImage* 9.2 (1999), pp. 179–194. DOI: 10.1006/nimg.1998.0395.

[39] Pierre Del Moral. "Nonlinear filtering: Interacting particle resolution". In: *Comptes Rendus de l'Académie des Sciences - Series I - Mathematics* 325.6 (1997), pp. 653–658. DOI: 10.1016/S0764-4442(97)84778-7.

[40] Flavio Dell'Acqua and Jacques-Donald Tournier. "Modelling white matter with spherical deconvolution: How and why?" In: *NMR in Biomedicine* 32.4 (2018). DOI: 10.1002/nbm.3945.

[41] Maxime Descoteaux, Elaine Angelino, Shaun Fitzgibbons, and Rachid Deriche. "Apparent diffusion coefficients from high angular resolution diffusion imaging: Estimation and applications". In: *Magnetic Resonance in Medicine* 56.2 (2006), pp. 395–410. DOI: 10.1002/mrm.20948.

[42] Maxime Descoteaux, Rachid Deriche, Thomas R. Knosche, and Alfred Anwander. "Deterministic and Probabilistic Tractography Based on Complex Fibre Orientation Distributions". en. In: *IEEE Transactions on Medical Imaging* 28.2 (Feb. 2009), pp. 269–286. DOI: 10.1109/TMI.2008.2004424.

[43] Bibek Dhital, Marco Reisert, Elias Kellner, and Valerij G. Kiselev. "Intra-axonal diffusivity in brain white matter". en. In: *NeuroImage* 189 (Apr. 2019), pp. 543–550. DOI: 10.1016/j.neuroimage.2019.01.015.

[44] J.R. Driscoll and Dennis M. Healy. "Computing Fourier Transforms and Convolutions on the 2-Sphere". In: *Advances in Applied Mathematics* 15.2 (1994), pp. 202–250. DOI: 10.1006/aama.1994.1008.

[45] Christian Ewert, David Kügler, Anastasia Yendiki, and Martin Reuter. "Learning Anatomical Segmentationsfor Tractography from Diffusion MRI". en. In: *Computational Diffusion MRI*. Ed. by Noemi Gyori, Jana Hutter, Vishwesh Nath, Marco Palombo, Marco Pizzolato, and Fan Zhang. Series Title: Mathematics and Visualization. Cham: Springer International Publishing, 2021, pp. 81–93. DOI: 10.1007/978-3-030-73018-5_7.

[46] Yuanjing Feng and Jianzhong He. "Asymmetric fiber trajectory distribution estimation using streamline differential equation". en. In: *Medical Image Analysis* 63 (July 2020), p. 101686. DOI: 10.1016/j.media.2020.101686.

[47] Gerd Fischer. *Lineare Algebra: Eine Einführung für Studienanfänger*. Springer-Verlag, Nov. 2013. DOI: 10.1007/978-3-662-61645-1.

[48] Bruce Fischl, André van der Kouwe, Christophe Destrieux, Eric Halgren, Florent Ségonne, David H. Salat, Evelina Busa, Larry J. Seidman, Jill Goldstein, David Kennedy, Verne Caviness, Nikos Makris, Bruce Rosen, and Anders M. Dale. "Automatically Parcellating the Human Cerebral Cortex". In: *Cerebral Cortex* 14.1 (2004), pp. 11–22. DOI: 10.1093/cercor/bhg087.

[49] Raisa Z. Freidlin, Evren Özarslan, Michael E. Komlosh, Lin-Ching Chang, Cheng Guan Koay, Derek K. Jones, and Peter J. Basser. "Parsimonious Model Selection for Tissue Segmentation and Classification Applications: A Study Using Simulated and Experimental DTI Data". In: *IEEE Trans. on Medical Imaging* 26.11 (2007), pp. 1576–1584. DOI: 10.1109/TMI.2007.907294.

[50] Milton Friedman. "The Use of Ranks to Avoid the Assumption of Normality Implicit in the Analysis of Variance". In: *Journal of the American Statistical Association* 32.200 (1937), pp. 675–701. DOI: 10.1080/01621459.1937.10503522.

[51] Josiah W. Gibbs. "Fourier's series". In: *Nature* 59.1522 (1898), pp. 200–200. DOI: 10.1038/059200b0.

[52] Christina Gillmann, Dorothee Saur, Thomas Wischgoll, and Gerik Scheuermann. "Uncertainty-aware Visualization in Medical Imaging - A Survey". In: *Computer Graphics Forum* 40.3 (2021), pp. 665–689. DOI: 10.1111/cgf.14333.

[53] Shun Gong, Fan Zhang, Isaiah Norton, Walid I. Essayed, Prashin Unadkat, Laura Rigolo, Ofer Pasternak, Yogesh Rathi, Lijun Hou, Alexandra J. Golby, and Lauren J. O'Donnell. "Free water modeling of peritumoral edema using multi-fiber tractography: Application to tracking the arcuate fasciculus for neurosurgical planning". en. In: *PLOS ONE* 13.5 (May 2018). Ed. by Pew-Thian Yap, e0197056. DOI: 10.1371/journal.pone.0197056.

[54] Andreas Graumann, Mirco Richter, Christopher Nimsky, and Dorit Merhof. "Exploring Crossing Fibers of the Brain's White Matter Using Directional Regions of Interest". In: *Visualization in Medicine and Life Sciences III*. Springer, 2016, pp. 179–194. DOI: 10.1007/978-3-319-24523-2_8.

[55] Robin Green. "Spherical Harmonic Lighting: The Gritty Details". In: *Archives of the game developers conference* 56 (2003), p. 4.

[56] Vijay P. B. Grover, Joshua M. Tognarelli, Mary M. E. Crossey, I. Jane Cox, Simon D. Taylor-Robinson, and Mark J. W. McPhail. "Magnetic Resonance Imaging: Principles and Techniques: Lessons for Clinicians". eng. In: *Journal of Clinical and Experimental Hepatology* 5.3 (Sept. 2015), pp. 246–255. DOI: 10.1016/j.jceh.2015.08.001.

[57] Johannes Grün, Samuel Gröschel, and Thomas Schultz. "Spatially Regularized Low-Rank Tensor Approximation for Accurate and Fast Tractography". In: *NeuroImage* 271 (2023). DOI: 10.1016/j.neuroimage.2023.120004.

[58] Johannes Grün, Jonah Sieg, and Thomas Schultz. "Anisotropic Fanning Aware Low-Rank Tensor Approximation Based Tractography". In: (2023). preprint, reviewed version will be published in proceedings of MICCAI CDMRI workshop. DOI: 10.48550/arXiv.2307.00833.

[59] Johannes Grün, Gemma van der Voort, and Thomas Schultz. "Model Averaging and Bootstrap Consensus Based Uncertainty Reduction in Diffusion MRI Tractography". In: *Computer Graphics Forum* 42.1 (2023), pp. 217–230. DOI: 10.1111/cgf.14724.

[60] Johannes Grün, Gemma van der Voort, and Thomas Schultz. "Reducing Model Uncertainty in Crossing Fiber Tractography". In: Proc. EG Workshop on Visual Computing for Biology and Medicine (VCBM). 2021, pp. 55–64. DOI: 10.2312/vcbm.20211345.

[61] Mario Hlawitschka and Gerik Scheuermann. "HOT-Lines: Tracking Lines in Higher Order Tensor Fields". In: *Proc. IEEE Visualization*. Ed. by C. Silva, E. Gröller, and H. Rushmeier. 2005, pp. 27–34. DOI: 10.1109/VISUAL.2005.1532773.

[62] Susie Y. Huang, Thomas Witzel, Boris Keil, Alina Scholz, Mathias Davids, Peter Dietz, Elmar Rummert, Rebecca Ramb, John E. Kirsch, Anastasia Yendiki, Qiuyun Fan, Qiyuan Tian, Gabriel Ramos-Llordén, Hong-Hsi Lee, Aapo Nummenmaa, Berkin Bilgic, Kawin Setsompop, Fuyixue Wang, Alexandru V. Avram, Michal Komlosh, Dan Benjamini, Kulam Najmudeen Magdoom, Sudhir Pathak, Walter Schneider, Dmitry S. Novikov, Els Fieremans, Slimane Tounekti, Choukri Mekkaoui, Jean Augustinack, Daniel Berger, Alexander Shapson-Coe, Jeff Lichtman, Peter J. Basser, Lawrence L. Wald, and Bruce R. Rosen. "Connectome 2.0: Developing the next-generation ultra-high gradient strength human MRI scanner for bridging studies of the micro-, meso- and macro-connectome". In: *NeuroImage* 243 (2021), p. 118530. DOI: 10.1016/j.neuroimage.2021.118530.

[63] Daniel P. Huttenlocher, G.A. Klanderman, and William J. Rucklidge. "Comparing images using the Hausdorff distance". In: *IEEE Transactions on Pattern Analysis and Machine Intelligence* 15.9 (1993), pp. 850–863. DOI: 10.1109/34.232073.

[64] S. Rao Jammalamadaka and György H. Terdik. "Harmonic analysis and distribution-free inference for spherical distributions". In: *Journal of Multivariate Analysis* 171 (2019), pp. 436–451. DOI: 10.1016/j.jmva.2019.01.012.

[65] Saad Jbabdi, Pierre Bellec, Roberto Toro, Jeab Daunizeau, M. Pélégrini-Issac, and Habib Benali. "Accurate Anisotropic Fast Marching for Diffusion-Based Geodesic Tractography". en. In: *International Journal of Biomedical Imaging* 2008 (2008), pp. 1–12. DOI: 10.1155/2008/320195.

[66] Mark Jenkinson, Peter Bannister, Michael Brady, and Stephen Smith. "Improved Optimization for the Robust and Accurate Linear Registration and Motion Correction of Brain Images". In: *NeuroImage* 17.2 (2002), pp. 825–841. DOI: 10.1006/nimg.2002.1132.

[67] Mark Jenkinson, Christian F. Beckmann, Timothy E.J. Behrens, Mark W. Woolrich, and Stephen M. Smith. "FSL". In: *NeuroImage* 62.2 (2012), pp. 782–790. DOI: 10.1016/j.neuroimage.2011.09.015.

[68] Ellen C. Jensen. "Technical Review, Types of Imaging, Part 4—Magnetic Resonance Imaging". In: *The Anatomical Record* 297.6 (2014), pp. 973–978. DOI: 10.1002/ar.22927.

[69] Jens H. Jensen, Joseph A. Helpern, Anita Ramani, Hanzhang Lu, and Kyle Kaczynski. "Diffusional Kurtosis Imaging: The Quantification of Non-Gaussian Water Diffusion by Means of Magnetic Resonance Imaging". In: *Magnetic Resonance in Medicine* 53 (2005), pp. 1432–1440. DOI: 10.1002/mrm.20508.

[70] Ben Jeurissen, Maxime Descoteaux, Susumu Mori, and Alexander Leemans. "Diffusion MRI fiber tractography of the brain". In: *NMR in Biomedicine* 32.4 (2019), e3785. DOI: 10.1002/nbm.3785.

[71] Ben Jeurissen, Alexander Leemans, Derek K. Jones, Jacques-Donald Tournier, and Jan Sijbers. "Probabilistic Fiber Tracking Using the Residual Bootstrap with Constrained Spherical Deconvolution". In: *Human Brain Mapping* 32 (2011), pp. 461–479. DOI: 10.1002/hbm.21032.

[72] Ben Jeurissen, Alexander Leemans, Jacques-Donald Tournier, Derek Jones, and Jan Sijbers. "Estimating the Number of Fiber Orientations in Diffusion MRI Voxels: A Constrained Spherical Deconvolution Study". In: *Proc. Intl. Soc. Mag. Reson. Med.* 18 (Jan. 2010).

[73] Ben Jeurissen, Alexander Leemans, Jacques-Donald Tournier, Derek K. Jones, and Jan Sijbers. "Investigating the prevalence of complex fiber configurations in white matter tissue with diffusion magnetic resonance imaging". In: *Human Brain Mapping* 34.11 (2012), pp. 2747–2766. DOI: 10.1002/hbm.22099.

[74] Ben Jeurissen, Jacques-Donald Tournier, Thijs Dhollander, Alan Connelly, and Jan Sijbers. "Multi-tissue constrained spherical deconvolution for improved analysis of multi-shell diffusion MRI data". In: *NeuroImage* 103 (2014), pp. 411–426. DOI: 10.1016/j.neuroimage.2014.07.061.

[75] Derek K. Jones. "Determining and visualizing uncertainty in estimates of fiber orientation from diffusion tensor MRI". en. In: *Magnetic Resonance in Medicine* 49.1 (2003), pp. 7–12. DOI: 10.1002/mrm.10331.

[76] Derek K. Jones. "The effect of gradient sampling schemes on measures derived from diffusion tensor MRI: a Monte Carlo study". eng. In: *Magnetic Resonance in Medicine* 51.4 (Apr. 2004), pp. 807–815. DOI: 10.1002/mrm.20033.

[77] Derek K. Jones. "Tractography Gone Wild: Probabilistic Fibre Tracking Using the Wild Bootstrap With Diffusion Tensor MRI". In: *IEEE Transactions on Medical Imaging* 27.9 (2008), pp. 1268–1274. DOI: 10.1109/TMI.2008.922191.

[78] Derek K. Jones, Adam R. Travis, Greg Eden, Carlo Pierpaoli, and Peter J. Basser. "PASTA: Pointwise assessment of streamline tractography attributes". In: *Magnetic Resonance in Medicine* 53.6 (2005), pp. 1462–1467. DOI: 10.1002/mrm.20484.

[79] Simon J. Julier and Jeffrey K. Uhlmann. "New extension of the Kalman filter to nonlinear systems". In: *Signal Processing, Sensor Fusion, and Target Recognition VI*. Ed. by Ivan Kadar. Vol. 3068. International Society for Optics and Photonics. SPIE, 1997, pp. 182–193. DOI: 10.1117/12.280797.

[80] Simon J. Julier and Jeffrey K. Uhlmann. "Reduced sigma point filters for the propagation of means and covariances through nonlinear transformations". In: *Proceedings of the 2002 American Control Conference (IEEE Cat. No.CH37301)*. Vol. 2. 2002, pp. 887–892. DOI: 10.1109/ACC.2002.1023128.

[81] Simon J. Julier and Jeffrey K. Uhlmann. "Unscented filtering and nonlinear estimation". In: *Proceedings of the IEEE* 92.3 (2004), pp. 401–422. DOI: 10.1109/JPROC.2003.823141.

[82] Simon J. Julier, Jeffrey K. Uhlmann, and Hugh F. Durrant-Whyte. "A new approach for filtering nonlinear systems". In: *Proceedings of 1995 American Control Conference - ACC'95*. Vol. 3. 1995, pp. 1628–1632. DOI: 10.1109/ACC.1995.529783.

[83] Peter E. Jupp and Kanti V. Mardia. *Statistics of Directional Data*. Wiley, 1999. DOI: 10.1111/j.2517-6161.1975.tb01550.x.

[84] Enrico Kaden, Thomas R. Knösche, and Alfred Anwander. "Parametric spherical deconvolution: Inferring anatomical connectivity using diffusion MR imaging". In: *NeuroImage* 37 (2007), pp. 474–488. DOI: 10.1016/j.neuroimage.2007.05.012.

[85] Rudolf E. Kalman. "A New Approach to Linear Filtering and Prediction Problems". In: *J. Fluids Eng.* 82.1 (1960), pp. 35–45. DOI: 10.1115/1.3662552.

[86] Elias Kellner, Bibek Dhital, Valerij G. Kiselev, and Marco Reisert. "Gibbs-ringing artifact removal based on local subvoxel-shifts". In: *Magnetic resonance in medicine* 76.5 (2016), pp. 1574–1581. DOI: 10.1002/mrm.26054.

[87] Alexandra Koch, Andrei Zhukov, Tony Stöcker, Samuel Groeschel, and Thomas Schultz. "SHORE-based detection and imputation of dropout in diffusion MRI". eng. In: *Magnetic Resonance in Medicine* 82.6 (Dec. 2019), pp. 2286–2298. DOI: 10.1002/mrm.27893.

[88] Sadanori Konishi and Genshiro Kitagawa. *Information Criteria and Statistical Modeling*. Springer Science & Business Media, 2008. DOI: 10.1007/978-0-387-71887-3.

[89] Lidia Konopleva, Kamil A. Il'yasov, Henrik Skibbe, Valerij G. Kiselev, Elias Kellner, Bibek Dhital, and Marco Reisert. "Modelfree global tractography". In: *NeuroImage* 174 (2018), pp. 576–586. DOI: 10.1016/j.neuroimage.2018.03.058.

[90] Simon Koppers and Dorit Merhof. "Direct Estimation of Fiber Orientations Using Deep Learning in Diffusion Imaging". In: *Machine Learning in Medical Imaging*. Ed. by Li Wang, Ehsan Adeli, Qian Wang, Yinghuan Shi, and Heung-Il Suk. Cham: Springer International Publishing, 2016, pp. 53–60. DOI: 10.1007/978-3-319-47157-0_7.

[91] Edgar Kraft. "A quaternion-based unscented Kalman filter for orientation tracking". In: *Sixth International Conference of Information Fusion, 2003. Proceedings of the*. Vol. 1. 2003, pp. 47–54. DOI: 10.1109/ICIF.2003.177425.

[92] Björn W. Kreher, Irina Mader, and Valerij G. Kiselev. "Gibbs tracking: A novel approach for the reconstruction of neuronal pathways". In: *Magnetic Resonance in Medicine* 60.4 (2008), pp. 953–963. DOI: 10.1002/mrm.21749.

[93] Poondi Kumaraswamy. "A generalized probability density function for double-bounded random processes". In: *Journal of Hydrology* 46.1-2 (1980), pp. 79–88. DOI: 10.1016/0022-1694(80)90036-0.

[94] Ernst Eduard Kummer. "De integralibus quibusdam definitis et seriebus infinitis". In: *Journal für die reine und angewandte Mathematik* 17 (1837), pp. 228–242. DOI: 10.1515/crll.1837.17.228.

[95] Hanna Küpper, Samuel Groeschel, Michael Alber, Uwe Klose, Martin U Schuhmann, and Marko Wilke. "Comparison of different tractography algorithms and validation by intraoperative stimulation in a child with a brain tumor". In: *Neuropediatrics* 46.1 (2015), pp. 72–75. DOI: 10.1055/s-0034-1395346.

[96] Björn Lampinen, Filip Szczepankiewicz, Jimmy Lätt, Linda Knutsson, Johan Mårtensson, Isabella M. Björkman-Burtscher, Danielle van Westen, Pia C. Sundgren, Freddy Ståhlberg, and Markus Nilsson. "Probing brain tissue microstructure with MRI: principles, challenges, and the role of multidimensional diffusion-relaxation encoding". In: *NeuroImage* 282 (Nov. 2023), p. 120338. DOI: 10.1016/j.neuroimage.2023.120338.

[97] Mariana Lazar and Andrew L. Alexander. "Bootstrap white matter tractography (BOOT-TRAC)". en. In: *NeuroImage* 24.2 (Jan. 2005), pp. 524–532. DOI: 10.1016/j.neuroimage.2004.08.050.

[98] Denis Le Bihan, Eric Breton, Denis Lallemand, Philippe Grenier, Emmanuel Cabanis, and Maurice Laval-Jeantet. "MR Imaging of Intravoxel Incoherent Motions: Application to Diffusion and Perfusion in Neurologic Disorders". In: *Radiology* 161.2 (1986), pp. 401–407. DOI: 10.1148/radiology.161.2.3763909.

[99] Zhichao Lin, Ting Gong, Kewen Wang, Zhiwei Li, Hongjian He, Qiqi Tong, Feng Yu, and Jianhui Zhong. "Fast learning of fiber orientation distribution function for MR tractography using convolutional neural network". In: *Medical Physics* 46.7 (2019), pp. 3101–3116. DOI: 10.1002/mp.13555.

[100] Klaus H. Maier-Hein, Peter F. Neher, Jean-Christophe Houde, Marc-Alexandre Côté, Eleftherios Garyfallidis, Jidan Zhong, Maxime Chamberland, Fang-Cheng Yeh, Ying-Chia Lin, Qing Ji, Wilburn E. Reddick, John O. Glass, David Qixiang Chen, Yuanjing Feng, Chengfeng Gao, Ye Wu, Jieyan Ma, Renjie He, Qiang Li, Carl-Fredrik Westin, Samuel Deslauriers-Gauthier, J. Omar Ocegueda González, Michael Paquette, Samuel St-Jean, Gabriel Girard, François Rheault, Jasmeen Sidhu, Chantal M. W. Tax, Fenghua Guo, Hamed Y. Mesri, Szabolcs Dávid, Martijn Froeling, Anneriet M. Heemskerk, Alexander Leemans, Arnaud Boré, Basile Pinsard, Christophe Bedetti, Matthieu Desrosiers, Simona Brambati, Julien Doyon, Alessia Sarica, Roberta Vasta, Antonio Cerasa, Aldo Quattrone, Jason Yeatman, Ali R. Khan, Wes Hodges, Simon Alexander, David Romascano, Muhamed Barakovic, Anna Auría, Oscar Esteban, Alia Lemkaddem, Jean-Philippe Thiran, H. Ertan Cetingul, Benjamin L. Odry, Boris Mailhe, Mariappan S. Nadar, Fabrizio Pizzagalli, Gautam Prasad, Julio E. Villalon-Reina, Justin Galvis, Paul M. Thompson, Francisco De Santiago Requejo, Pedro Luque Laguna, Luis Miguel Lacerda, Rachel Barrett, Flavio Dell'Acqua, Marco Catani, Laurent Petit, Emmanuel Caruyer, Alessandro Daducci, Tim B. Dyrby, Tim Holland-Letz, Claus C. Hilgetag, Bram Stieltjes, and Maxime Descoteaux. "The challenge of mapping the human connectome based on diffusion tractography". In: *Nature Communications* 8.1 (2017). DOI: 10.1038/s41467-017-01285-x.

[101] James Malcolm, Martha Shenton, and Yogesh Rathi. "Filtered multitensor tractography". In: *IEEE Transactions on Medical Imaging* 29 (Sept. 2010), pp. 1664–75. DOI: 10.1109/TMI.2010.2048121.

[102] James G. Malcolm, Oleg Michailovich, Sylvain Bouix, Carl-Fredrik Westin, Martha E. Shenton, and Yogesh Rathi. "A filtered approach to neural tractography using the Watson directional function". In: *Medical Image Analysis* 14.1 (2010), pp. 58–69. DOI: 10.1016/j.media.2009.10.003.

[103] Jean-François Mangin, Cyril Poupon, Yann Cointepas, Denis Rivière, Dimitri Papadopoulos-Orfanos, Chris A. Clark, Jean Régis, and Denis Le Bihan. "A framework based on spin glass models for the inference of anatomical connectivity from diffusion-weighted MR data - a technical review". en. In: *NMR in Biomedicine* 15.7-8 (2002), pp. 481–492. DOI: 10.1002/nbm.780.

[104] Kanti V Mardia and Peter E Jupp. *Directional statistics*. Vol. 494. John Wiley & Sons, 2009. DOI: 10.1002/9780470316979.

[105] Kenneth Marek, Danna Jennings, Shirley Lasch, Andrew Siderowf, Caroline Tanner, Tanya Simuni, Chris Coffey, Karl Kieburtz, Emily Flagg, Sohini Chowdhury, Werner Poewe, Brit Mollenhauer, Paracelsus-Elena Klinik, Todd Sherer, Mark Frasier, Claire Meunier, Alice Rudolph, Cindy Casaceli, John Seibyl, Susan Mendick, Norbert Schuff, Ying Zhang, Arthur Toga, Karen Crawford, Alison Ansbach, Pasquale De Blasio, Michele Piovella, John Trojanowski, Les Shaw, Andrew Singleton, Keith Hawkins, Jamie Eberling, Deborah Brooks, David Russell, Laura Leary, Stewart Factor, Barbara Sommerfeld, Penelope Hogarth, Emily Pighetti, Karen Williams, David Standaert, Stephanie Guthrie, Robert Hauser, Holly Delgado, Joseph Jankovic, Christine Hunter, Matthew Stern, Baochan Tran, Jim Leverenz, Marne Baca, Sam Frank, Cathi-Ann Thomas, Irene Richard, Cheryl Deeley, Linda Rees, Fabienne Sprenger, Elisabeth Lang, Holly Shill, Sanja Obradov, Hubert Fernandez, Adrienna Winters, Daniela Berg, Katharina Gauss, Douglas Galasko, Deborah Fontaine, Zoltan Mari, Melissa Gerstenhaber, David Brooks, Sophie Malloy, Paolo Barone, Katia Longo, Tom Comery, Bernard Ravina, Igor Grachev, Kim Gallagher, Michelle Collins, Katherine L. Widnell, Suzanne Ostrowizki, Paulo Fontoura, Tony Ho, Johan Luthman, Marcel van der Brug, Alastair D. Reith, and Peggy Taylor. “The Parkinson Progression Marker Initiative (PPMI)”. In: *Progress in Neurobiology* 95.4 (2011). Biological Markers for Neurodegenerative Diseases, pp. 629–635. DOI: 10.1016/j.pneurobio.2011.09.005.

[106] Simone Mastrogiacomo, Weiqiang Dou, John A. Jansen, and X. Frank Walboomers. “Magnetic Resonance Imaging of Hard Tissues and Hard Tissue Engineered Bio-substitutes”. eng. In: *Molecular Imaging and Biology* 21.6 (Dec. 2019), pp. 1003–1019. DOI: 10.1007/s11307-019-01345-2.

[107] Tomas Möller and Ben Trumbore. “Fast, Minimum Storage Ray-Triangle Intersection”. In: *Journal of Graphics Tools* 2.1 (1997), pp. 21–28. DOI: 10.1080/10867651.1997.10487468.

[108] Susumu Mori, Barbara J. Crain, V. P. Chacko, and Peter C. M. van Zijl. “Three-dimensional tracking of axonal projections in the brain by magnetic resonance imaging”. In: *Annals of Neurology* 45.2 (1999), pp. 265–269. DOI: 10.1002/1531-8249(199902)45:2<265::aid-ana21>3.0.co;2-3.

[109] Bryon A. Mueller, Kelvin O. Lim, Laura Hemmy, and Jazmin Camchong. “Diffusion MRI and its Role in Neuropsychology”. eng. In: *Neuropsychology Review* 25.3 (Sept. 2015), pp. 250–271. DOI: 10.1007/s11065-015-9291-z.

[110] Vishwesh Nath, Ilwoo Lyu, Kurt G. Schilling, Prasanna Parvathaneni, Colin B. Hansen, Yuankai Huo, Vaibhav A. Janve, Yurui Gao, Iwona Stepniewska, Adam W. Anderson, and Bennett A. Landman. “Enabling Multi-shell b-Value Generalizability of Data-Driven Diffusion Models with Deep SHORE”. In: *Medical Image Computing and Computer Assisted Intervention – MICCAI 2019*. Ed. by Dinggang Shen, Tianming Liu, Terry M. Peters, Lawrence H. Staib, Caroline Essert, Sean Zhou, Pew-Thian Yap, and Ali Khan. Cham: Springer International Publishing, 2019, pp. 573–581. DOI: 10.1007/978-3-030-32248-9_64.

[111] Vishwesh Nath, Kurt G. Schilling, Prasanna Parvathaneni, Colin B. Hansen, Allison E. Hainline, Yuankai Huo, Justin A. Blaber, Ilwoo Lyu, Vaibhav Janve, Yurui Gao, Iwona Stepniewska, Adam W. Anderson, and Bennett A. Landman. “Deep learning reveals untapped information for local white-matter fiber

reconstruction in diffusion-weighted MRI". In: *Magnetic Resonance Imaging* 62 (2019), pp. 220–227. DOI: 10.1016/j.mri.2019.07.012.

[112] Peter F. Neher, Marc-Alexandre Côté, Jean-Christophe Houde, Maxime Descoteaux, and Klaus H. Maier-Hein. "Fiber tractography using machine learning". en. In: *NeuroImage* 158 (Sept. 2017), pp. 417–429. DOI: 10.1016/j.neuroimage.2017.07.028.

[113] Peter F. Neher, Maxime Descoteaux, Jean-Christophe Houde, Bram Stieltjes, and Klaus H. Maier-Hein. "Strengths and weaknesses of state of the art fiber tractography pipelines. A comprehensive in-vivo and phantom evaluation study using Tractometer". In: *Medical Image Analysis* 26.1 (2015), pp. 287–305. DOI: 10.1016/j.media.2015.10.011.

[114] Peter B. Nemenyi. "DistributionFree Multiple Comparison". PhD thesis. Princeton University, 1963.

[115] Evren Özarslan and Thomas H. Mareci. "Generalized diffusion tensor imaging and analytical relationships between diffusion tensor imaging and high angular resolution diffusion imaging". In: *Magnetic Resonance in Medicine* 50.5 (2003), pp. 955–965. DOI: 10.1002/mrm.10596.

[116] Eleftheria Panagiotaki, Torben Schneider, Bernard Siow, Matt G. Hall, Mark F. Lythgoe, and Daniel C. Alexander. "Compartment models of the diffusion MR signal in brain white matter: A taxonomy and comparison". In: *NeuroImage* 59 (2012), pp. 2241–54. DOI: 10.1016/j.neuroimage.2011.09.081.

[117] Anand S. Pandit, Gareth Ball, A. David Edwards, and Serena J. Counsell. "Diffusion magnetic resonance imaging in preterm brain injury". eng. In: *Neuroradiology* 55 Suppl 2 (Sept. 2013), pp. 65–95. DOI: 10.1007/s00234-013-1242-x.

[118] Kanil Patel, Samuel Groeschel, and Thomas Schultz. "Better Fiber ODFs from Suboptimal Data with Autoencoder Based Regularization". In: *Medical Image Computing and Computer Assisted Intervention - MICCAI 2018: 21st International Conference, Granada, Spain, September 16-20, 2018, Proceedings, Part III*. Berlin, Heidelberg: Springer-Verlag, Sept. 2018, pp. 55–62. DOI: 10.1007/978-3-030-00931-1_7.

[119] Philippe Poulin, Marc-Alexandre Côté, Jean-Christophe Houde, Laurent Petit, Peter F. Neher, Klaus H. Maier-Hein, Hugo Larochelle, and Maxime Descoteaux. "Learn to Track: Deep Learning for Tractography". In: *Medical Image Computing and Computer Assisted Intervention - MICCAI 2017*. Ed. by Maxime Descoteaux, Lena Maier-Hein, Alfred Franz, Pierre Jannin, D. Louis Collins, and Simon Duchesne. Cham: Springer International Publishing, 2017, pp. 540–547. DOI: 10.1007/978-3-319-66182-7_62.

[120] Philippe Poulin, Daniel Jörgens, Pierre-Marc Jodoin, and Maxime Descoteaux. "Tractography and machine learning: Current state and open challenges". In: *Magnetic Resonance Imaging* 64 (2019), pp. 37–48. DOI: 10.1016/j.mri.2019.04.013.

[121] Arish A. Qazi, Alireza Radmanesh, Lauren O'Donnell, Gordon Kindlmann, Sharon Peled, Carl-Fredrik Westin, and Alexandra J. Golby. "Resolving Crossings in the Corticospinal Tract by Two-Tensor Streamline Tractography: Method and clinical assessment using fMRI". In: *NeuroImage* 47.2 (2009), T98–T106. DOI: 10.1016/j.neuroimage.2008.06.034.

[122] Yogesh Rathi, Borjan Gagoski, Kawin Setsompop, Oleg Michailovich, Patricia Grant, and Carl-Fredrik Westin. "Diffusion Propagator Estimation from Sparse Measurements in a Tractography Framework". In: vol. 16. Sept. 2013, pp. 510–7. DOI: 10.1007/978-3-642-40760-4_64.

[123] Chinthala P. Reddy and Yogesh Rathi. "Joint Multi-Fiber NODDI Parameter Estimation and Tractography Using the Unscented Information Filter". In: *Frontiers in Neuroscience* 10 (2016). DOI: 10.3389/fnins.2016.00166.

[124] Marco Reisert, Irina Mader, Constantin Anastasopoulos, Matthias Weigel, Susanne Schnell, and Valerij G. Kiselev. "Global fiber reconstruction becomes practical". en. In: *NeuroImage* 54.2 (Jan. 2011), pp. 955–962. DOI: 10.1016/j.neuroimage.2010.09.016.

[125] Till W. Riffert, Jan Schreiber, Alfred Anwander, and Thomas R. Knösche. "Beyond fractional anisotropy: Extraction of bundle-specific structural metrics from crossing fiber models". In: *NeuroImage* 100 (2014), pp. 176–191. DOI: 10.1016/j.neuroimage.2014.06.015.

[126] Timo Roine, Ben Jeurissen, Daniele Perrone, Jan Aelterman, Alexander Leemans, Wilfried Philips, and Jan Sijbers. "Isotropic non-white matter partial volume effects in constrained spherical deconvolution". In: *Frontiers in Neuroinformatics* 8 (2014). DOI: 10.3389/fninf.2014.00028.

[127] Paul-Noel Rousseau, M. Mallar Chakravarty, and Christopher J. Steele. "Mapping pontocerebellar connectivity with diffusion MRI". In: *NeuroImage* 264 (2022), p. 119684. DOI: 10.1016/j.neuroimage.2022.119684.

[128] Tabinda Sarwar, Caio Seguin, Kotagiri Ramamohanarao, and Andrew Zalesky. "Towards deep learning for connectome mapping: A block decomposition framework". en. In: *NeuroImage* 212 (May 2020), p. 116654. DOI: 10.1016/j.neuroimage.2020.116654.

[129] Simona Schiavi, Mario Ocampo-Pineda, Muhamed Barakovic, Laurent Petit, Maxime Descoteaux, Jean-Philippe Thiran, and Alessandro Daducci. "A new method for accurate in vivo mapping of human brain connections using microstructural and anatomical information". en. In: *Science Advances* 6.31 (July 2020), eaba8245. DOI: 10.1126/sciadv.aba8245.

[130] Kurt G. Schilling, Alessandro Daducci, Klaus Maier-Hein, Cyril Poupon, Jean-Christophe Houde, Vishwesh Nath, Adam W. Anderson, Bennett A. Landman, and Maxime Descoteaux. "Challenges in diffusion MRI tractography Lessons learned from international benchmark competitions". In: *Magnetic Resonance Imaging* 57 (2019), pp. 194–209. DOI: 10.1016/j.mri.2018.11.014.

[131] Kurt G. Schilling, Chantal M. W. Tax, Francois Rheault, Bennett A. Landman, Adam W. Anderson, Maxime Descoteaux, and Laurent Petit. "Prevalence of white matter pathways coming into a single white matter voxel orientation: The bottleneck issue in tractography". In: *Human Brain Mapping* 43.4 (2022), pp. 1196–1213. DOI: 10.1002/hbm.25697.

[132] Jan Schreiber, Till Riffert, Alfred Anwander, and Thomas R. Knösche. "Plausibility Tracking: A method to evaluate anatomical connectivity and microstructural properties along fiber pathways". en. In: *NeuroImage* 90 (Apr. 2014), pp. 163–178. DOI: 10.1016/j.neuroimage.2014.01.002.

[133] Thomas Schultz. "Learning a Reliable Estimate of the Number of Fiber Directions in Diffusion MRI". In: *Proc. Medical Image Computing and Computer-Assisted Intervention (MICCAI) Part III*. Ed. by N. Ayache et al. Vol. 7512. LNCS. 2012, pp. 493–500. DOI: 10.1007/978-3-642-33454-2_61.

[134] Thomas Schultz and Samuel Groeschel. "Auto-calibrating Spherical Deconvolution Based on ODF Sparsity". In: *Proc. Medical Image Computing and Computer-Assisted Intervention (MICCAI) Part I*. Ed. by K. Mori et al. Vol. 8149. LNCS. Springer, 2013, pp. 663–670. DOI: 10.1007/978-3-642-40811-3_83.

[135] Thomas Schultz and Gordon Kindlmann. "A Maximum Enhancing Higher-Order Tensor Glyph". In: *Computer Graphics Forum* 29.3 (2010), pp. 1143–1152. DOI: 10.1111/j.1467-8659.2009.01675.x.

[136] Thomas Schultz, Lara Schlaffke, Bernhard Schölkopf, and Tobias Schmidt-Wilcke. "HiFiVE: A Hilbert Space Embedding of Fiber Variability Estimates for Uncertainty Modeling and Visualization". In: *Computer Graphics Forum* 32.3 (2013), pp. 121–130. DOI: 10.1111/cgf.12099.

[137] Thomas Schultz and Hans-Peter Seidel. "Estimating Crossing Fibers: A Tensor Decomposition Approach". In: *IEEE Transactions on Visualization and Computer Graphics* 14.6 (2008), pp. 1635–1642. DOI: 10.1109/TVCG.2008.128.

[138] Thomas Schultz and Anna Vilanova. "Diffusion MRI Visualization". In: *NMR in Biomedicine* 32.4 (2019), e3902. DOI: 10.1002/nbm.3902.

[139] Thomas Schultz, Anna Vilanova, Ralph Brecheisen, and Gordon Kindlmann. "Fuzzy Fibers: Uncertainty in dMRI Tractography". In: *Scientific Visualization: Uncertainty, Multifield, Biomedical, and Scalable Visualization*. Ed. by C. Hansen, M. Chen, C. Johnson, A. Kaufman, and H. Hagen. Springer, 2014, pp. 79–92. DOI: 10.1007/978-1-4471-6497-5_8.

[140] Thomas Schultz, Carl-Fredrik Westin, and Gordon Kindlmann. "Multi-Diffusion-Tensor Fitting via Spherical Deconvolution: A Unifying Framework". In: *Proc. Medical Image Computing and Computer-Assisted Intervention (MICCAI)*. Ed. by Tianzi Jiang, Nassir Navab, Josien P. W. Pluim, and Max A. Viergever. Vol. 6361. LNCS. Springer, 2010, pp. 673–680. DOI: 10.1007/978-3-642-15705-9_82.

[141] Gideon Schwarz. "Estimating the Dimension of a Model". In: *The Annals of Statistics* 6.2 (Mar. 1978), pp. 461–464. DOI: 10.1214/aos/1176344136.

[142] Dmitri Shastin, Sila Genc, Greg D. Parker, Kristin Koller, Chantal M.W. Tax, John Evans, Khalid Hamandi, William P. Gray, Derek K. Jones, and Maxime Chamberland. "Surface-based tracking for short association fibre tractography". In: *NeuroImage* 260 (2022), p. 119423. DOI: 10.1016/j.neuroimage.2022.119423.

[143] Faizan Siddiqui, Thomas Höllt, and Anna Vilanova. "A Progressive Approach for Uncertainty Visualization in Diffusion Tensor Imaging". In: *Computer Graphics Forum* 40.3 (2021), pp. 411–422. DOI: 10.1111/cgf.14317.

[144] Robert E. Smith, Jacques-Donald Tournier, Fernando Calamante, and Alan Connelly. "SIFT: Spherical-deconvolution informed filtering of tractograms". en. In: *NeuroImage* 67 (Feb. 2013), pp. 298–312. DOI: 10.1016/j.neuroimage.2012.11.049.

[145] Robert E. Smith, Jacques-Donald Tournier, Fernando Calamante, and Alan Connelly. “SIFT2: Enabling dense quantitative assessment of brain white matter connectivity using streamlines tractography”. en. In: *NeuroImage* 119 (Oct. 2015), pp. 338–351. DOI: 10.1016/j.neuroimage.2015.06.092.

[146] Stamatios N. Sotiropoulos, Timothy E.J. Behrens, and Saad Jbabdi. “Ball and rackets: Inferring fiber fanning from diffusion-weighted MRI”. In: *NeuroImage* 60.2 (2012), pp. 1412–1425. DOI: 10.1016/j.neuroimage.2012.01.056.

[147] Stamatios N. Sotiropoulos, Saad Jbabdi, Junqian Xu, Jesper L. Andersson, Steen Moeller, Edward J. Auerbach, Matthew F. Glasser, Moises Hernandez, Guillermo Sapiro, Mark Jenkinson, David A. Feinberg, Essa Yacoub, Christophe Lenglet, David C. Van Essen, Kamil Ugurbil, and Timothy E.J. Behrens. “Advances in diffusion MRI acquisition and processing in the Human Connectome Project”. In: *NeuroImage* 80 (2013), pp. 125–143. DOI: 10.1016/j.neuroimage.2013.05.057.

[148] Suvrit Sra. “A short note on parameter approximation for von Mises-Fisher distributions – And a fast implementation of $I_s(x)$”. In: *Computational Statistics* 27 (2012), pp. 177–190. DOI: 10.1007/s00180-011-0232-x.

[149] Suvrit Sra and Dmitrii Karp. “The multivariate Watson distribution: Maximum-likelihood estimation and other aspects”. In: *Journal of Multivariate Analysis* 114 (2013), pp. 256–269. DOI: 10.1016/j.jmva.2012.08.010.

[150] Edward O. Stejskal and John E. Tanner. “Spin Diffusion Measurements: Spin Echoes in the Presence of a TimeDependent Field Gradient”. In: *The Journal of Chemical Physics* 42.1 (1965), pp. 288–292. DOI: 10.1063/1.1695690.

[151] Hiromasa Takemura, Cesar F. Caiafa, Brian A. Wandell, and Franco Pestilli. “Ensemble Tractography”. In: *PLoS Computational Biology* 12.2 (2016), e1004692. DOI: 10.1371/journal.pcbi.1004692.

[152] Chantal M.W. Tax, Matteo Bastiani, Jelle Veraart, Eleftherios Garyfallidis, and M. Okan Irfanoglu. “What’s new and what’s next in diffusion MRI preprocessing”. en. In: *NeuroImage* 249 (Apr. 2022), p. 118830. DOI: 10.1016/j.neuroimage.2021.118830.

[153] Jean-Philippe Thivierge and Gary F. Marcus. “The topographic brain: from neural connectivity to cognition”. In: *Trends in Neurosciences* 30.6 (2007), pp. 251–259. DOI: 10.1016/j.tins.2007.04.004.

[154] Alexandra Tobisch, Rüdiger Stirnberg, Robbert L. Harms, Thomas Schultz, Alard Roebroeck, Monique M. Breteler, and Tony Stöcker. “Compressed Sensing Diffusion Spectrum Imaging for Accelerated Diffusion Microstructure MRI in Long-Term Population Imaging”. In: *Frontiers in Neuroscience* 12 (2018), p. 650. DOI: 10.3389/fnins.2018.00650.

[155] Carlo Tomasi and Roberto Manduchi. “Bilateral Filtering for Gray and Color Images”. In: *Proc. Int’l Conf. on Computer Vision (ICCV)*. IEEE Computer Society, 1998, pp. 839–846. DOI: 10.1109/ICCV.1998.710815.

[156] Daniel Topgaard and Olle Söderman. “Experimental determination of pore shape and size using q-space NMR microscopy in the long diffusion-time limit”. In: *Magnetic Resonance Imaging* 21.1 (2003), pp. 69–76. DOI: 10.1016/S0730-725X(02)00626-4.

[157] Jacques-Donald Tournier, Fernando Calamante, and Alan Connelly. “Improved probabilistic streamlines tractography by 2nd order integration over fibre orientation distributions”. In: vol. 18. 2010.

[158] Jacques-Donald Tournier, Fernando Calamante, and Alan Connelly. "Robust determination of the fibre orientation distribution in diffusion MRI: Non-negativity constrained super-resolved spherical deconvolution". In: *NeuroImage* 35.4 (2007), pp. 1459–1472. DOI: https://doi.org/10.1016/j.neuroimage.2007.02.016.

[159] Jacques-Donald Tournier, Fernando Calamante, David G. Gadian, and Alan Connelly. "Direct estimation of the fiber orientation density function from diffusion-weighted MRI data using spherical deconvolution". In: *NeuroImage* 23.3 (2004), pp. 1176–1185. DOI: 10.1016/j.neuroimage.2004.07.037.

[160] Jacques-Donald Tournier, Robert Smith, David Raffelt, Rami Tabbara, Thijs Dhollander, Maximilian Pietsch, Daan Christiaens, Ben Jeurissen, Chun-Hung Yeh, and Alan Connelly. "MRtrix3: A fast, flexible and open software framework for medical image processing and visualisation". In: *NeuroImage* 202 (2019), p. 116137. DOI: 10.1016/j.neuroimage.2019.116137.

[161] David S. Tuch, Timothy G. Reese, Mette R. Wiegell, Nikos Makris, John W. Belliveau, and Van J. Wedeen. "High angular resolution diffusion imaging reveals intravoxel white matter fiber heterogeneity". In: *Magnetic Resonance in Medicine* 48.4 (), pp. 577–582. DOI: 10.1002/mrm.10268.

[162] Jeffrey K. Uhlmann and Simon J. Julier. "Gaussianity and the Kalman Filter: A Simple Yet Complicated Relationship". In: *Journal de Ciencia e Ingenieria* 14.1 (2022), pp. 21–26. DOI: 10.46571/JCI.2022.1.2.

[163] David C. Van Essen, Stephen M. Smith, Deanna M. Barch, Timothy E.J. Behrens, Essa Yacoub, and Kamil Ugurbil. "The WU-Minn Human Connectome Project: An overview". In: *NeuroImage* 80 (2013), pp. 62–79. DOI: 10.1016/j.neuroimage.2013.05.041.

[164] Andrea Vázquez, Narciso López-López, Alexis Sánchez, Josselin Houenou, Cyril Poupon, Jean-François Mangin, Cecilia Hernández, and Pamela Guevara. "FFClust: Fast fiber clustering for large tractography datasets for a detailed study of brain connectivity". In: *NeuroImage* 220 (2020), p. 117070. DOI: 10.1016/j.neuroimage.2020.117070.

[165] Jelle Veraart, Els Fieremans, and Dmitry Novikov. "Diffusion MRI noise mapping using random matrix theory". In: *Magnetic resonance in medicine* 76 (Nov. 2015), pp. 1582–1593. DOI: 10.1002/mrm.26059.

[166] Jelle Veraart, Dmitry Novikov, Daan Christiaens, Benjamin Ades-Aron, Jan Sijbers, and Els Fieremans. "Denoising of diffusion MRI using random matrix theory". In: *NeuroImage* 142 (Aug. 2016), pp. 394–406. DOI: 10.1016/j.neuroimage.2016.08.016.

[167] Sjoerd B. Vos, Max A. Viergever, and Alexander Leemans. "Multi-Fiber Tractography Visualizations for Diffusion MRI Data". In: *PLOS ONE* 8.11 (2013), e81453. DOI: 10.1371/journal.pone.0081453.

[168] Setsu Wakana, Arvind Caprihan, Martina M. Panzenboeck, James H. Fallon, Michele Perry, Randy L. Gollub, Kegang Hua, Jiangyang Zhang, Hangyi Jiang, Prachi Dubey, Ari Blitz, Petert van Zijl, and Susumu Mori. "Reproducibility of quantitative tractography methods applied to cerebral white matter". In: *NeuroImage* 36 (2007), pp. 630–644. DOI: 10.1016/j.neuroimage.2007.02.049.

[169] Zhou Wang, Alan C Bovik, Hamid R Sheikh, and Eero P Simoncelli. "Image quality assessment: from error visibility to structural similarity". In: *IEEE transactions on image processing* 13.4 (2004), pp. 600–612. DOI: 10.1109/TIP.2003.819861.

[170] Jakob Wasserthal, Peter Neher, and Klaus H. Maier-Hein. "TractSeg - Fast and accurate white matter tract segmentation". In: *NeuroImage* 183 (2018), pp. 239–253. DOI: 10.1016/j.neuroimage.2018.07.070.

[171] Jakob Wasserthal, Peter F. Neher, Dusan Hirjak, and Klaus H. Maier-Hein. "Combined tract segmentation and orientation mapping for bundle-specific tractography". en. In: *Medical Image Analysis* 58 (Dec. 2019), p. 101559. DOI: 10.1016/j.media.2019.101559.

[172] Geoffrey S. Watson. "Equatorial distributions on a sphere". In: *Biometrika* 52.1-2 (June 1965), pp. 193–202. DOI: 10.1093/biomet/52.1-2.193.

[173] Van J Wedeen, Patric Hagmann, Wen-Yih Tseng, Timothy G. Reese, and Robert M. Weisskoff. "Mapping complex tissue architecture with diffusion spectrum magnetic resonance imaging". In: *Magnetic Resonance in Medicine* 54 (2005). DOI: 10.1002/mrm.20642.

[174] Van J. Wedeen, R.P. Wang, Jeremy D. Schmahmann, T. Benner, Wen-Yih Tseng, Guangping Dai, D.N. Pandya, Patric Hagmann, Helen D'Arceuil, and A.J. de Crespigny. "Diffusion spectrum magnetic resonance imaging (DSI) tractography of crossing fibers". In: *NeuroImage* 41.4 (2008), pp. 1267–1277. DOI: 10.1016/j.neuroimage.2008.03.036.

[175] David Weinstein, Gordon Kindlmann, and Eric Lundberg. "Tensorlines: advection-diffusion based propagation through diffusion tensor fields". In: *Proc. IEEE Visualization*. 1999, pp. 249–253. DOI: 10.1109/VISUAL.1999.809894.

[176] Carl-Fredrik Westin, Filip Szczepankiewicz, Ofer Pasternak, Evren Özarslan, Daniel Topgaard, Hans Knutsson, and Markus Nilsson. "Measurement Tensors in Diffusion MRI: Generalizing the Concept of Diffusion Encoding". In: *Medical Image Computing and Computer-Assisted Intervention – MICCAI 2014*. Ed. by Polina Golland, Nobuhiko Hata, Christian Barillot, Joachim Hornegger, and Robert Howe. Cham: Springer International Publishing, 2014, pp. 209–216. DOI: 10.1007/978-3-319-10443-0_27.

[177] Brandon Whitcher, David S. Tuch, Jonathan J. Wisco, A. Gregory Sorensen, and Liqun Wang. "Using the wild bootstrap to quantify uncertainty in diffusion tensor imaging". en. In: *Human Brain Mapping* 29.3 (Mar. 2008), pp. 346–362. DOI: 10.1002/hbm.20395.

[178] Thomas Freud Wiener. "Theoretical analysis of gimballess inertial reference equipment using delta-modulated instruments". PhD thesis. Massachusetts Institute of Technology, 1962.

[179] Vitalis Wiens, Lara Schlaffke, Tobias Schmidt-Wilcke, and Thomas Schultz. "Visualizing Uncertainty in HARDI Tractography Using Superquadric Streamtubes". In: *Proc. EG Conf. on Visualization (EuroVis) Short Papers*. 2014, pp. 37–41. DOI: 10.2312/eurovisshort.20141154.

[180] Frank Wilcoxon. "Individual Comparisons by Ranking Methods". In: *Biometrics Bulletin* 1.6 (1945), pp. 80–83. DOI: 10.2307/3001968.

[181] Marko Wilke, Samuel Groeschel, Anna Lorenzen, Sabine Rona, Martin U. Schuhmann, Ulrike Ernemann, and Ingeborg Krägeloh-Mann. "Clinical application of advanced MR methods in children: points to consider". In: *Annals of Clinical and Translational Neurology* 5.11 (2018), pp. 1434–1455. DOI: 10.1002/acn3.658.

[182] Ernst Wit, Edwin van den Heuvel, and Jan-Willem Romeijn. ""All models are wrong...': an introduction to model uncertainty". In: *Statistica Neerlandica* 66.3 (2012), pp. 217–236. DOI: 10.1111/j.1467-9574.2012.00530.x.

[183] Max A. Woodbury. *Inverting modified matrices*. Statistical Research Group, Memo. Rep. no. 42, Princeton University, Princeton, NJ, 1950, p. 4.

[184] Weining Wu, Gloria Mcanulty, Hesham Hamoda, Kiera Sarill, Sarina Karmacharya, Borjan Gagoski, Lipeng Ning, Patricia Grant, Martha Shenton, Deborah Waber, Nikolaos Makris, and Yogesh Rathi. "Detecting microstructural white matter abnormalities of frontal pathways in children with ADHD using advanced diffusion models". In: *Brain Imaging and Behavior* 14 (2020), pp. 981–997. DOI: 10.1007/s11682-019-00108-5.

[185] Joseph Yuan-Mou Yang, Chun-Hung Yeh, Cyril Poupon, and Fernando Calamante. "Diffusion MRI tractography for neurosurgery: the basics, current state, technical reliability and challenges". In: *Physics in Medicine & Biology* 66.15 (2021), 15TR01. DOI: 10.1088/1361-6560/ac0d90.

[186] Hui Zhang, Torben Schneider, Claudia Gandini Wheeler-Kingshott, and Daniel Alexander. "NODDI: Practical in vivo neurite orientation dispersion and density imaging of the human brain". In: *NeuroImage* 61 (Mar. 2012), pp. 1000–16. DOI: 10.1016/j.neuroimage.2012.03.072.

[187] Song Zhang, Cagatay Demiralp, and David H. Laidlaw. "Visualizing Diffusion Tensor MR Images Using Streamtubes and Streamsurfaces". In: *IEEE Transactions on Visualization and Computer Graphics* 9.4 (2003), pp. 454–462. DOI: 10.1109/TVCG.2003.1260740.

[188] Yongyue Zhang, Michael Brady, and Stephen M. Smith. "Segmentation of brain MR images through a hidden Markov random field model and the expectation-maximization algorithm". In: *IEEE Transactions on Medical Imaging* 20.1 (2001), pp. 45–57. DOI: 10.1109/42.906424.

[189] Andreas Ziehe, Pavel Laskov, Guido Nolte, and Klaus-Robert Müller. "A Fast Algorithm for Joint Diagonalization with Non-orthogonal Transformations and its Application to Blind Source Separation". In: *J. Mach. Learn. Res.* 5 (2004), pp. 777–800.